Title

Signatures of Late Pleistocene fluvial incision in an Alpine landscape

Authors

Kerry Leith*[1,2], Matthew Fox[3], Jeffrey R. Moore[4,1]

*Corresponding author: kerry.leith@erdw.ethz.cha

Affiliations

[1]Geological Institute, ETH Zurich, Sonneggstrasse 5, 8092 Zurich, Switzerland

[2]Chair of Landslide Research, Technische Universität München, Arcisstrasse 21, 80333 Munich, Germany

[3]Department of Earth Sciences, University College London, Gower St., Kings Cross London, WC1E 6BT

[4]Geology and Geophysics, University of Utah, 115 South 1460, Salt Lake City, UT 84112-0102, USA

Abstract

Uncertainty regarding the relative efficacy of fluvial and glacial erosion has hindered attempts to quantitatively analyse the Pleistocene evolution of alpine landscapes. Here we show that the morphology of major tributaries of the Rhone River, Switzerland, is consistent with that predicted for a landscape shaped primarily by multiple phases of fluvial incision following a period of intense glacial erosion after the mid-Pleistocene transition (~0.7 Ma). This is despite major ice sheets reoccupying the region during cold intervals since the mid-Pleistocene. We use high-resolution LiDAR data to identify a series of convex reaches within the long-profiles of 18 tributary channels. We propose these reaches represent knickpoints, which developed as regional uplift raised tributary bedrock channels above the local fluvial baselevel during glacial intervals, and migrated upstream as the fluvial system was re-established during interglacial periods. Using a combination of integral long-profile analysis and stream-power modelling, we find that the locations of ~80% of knickpoints in our study region are consistent with that predicted for a fluvial origin, while the mean residual error over ~100 km of modelled channels is just 26.3 m. Breaks in cross-valley profiles project toward the elevation of former end-of-interglacial channel elevations, supporting our model results. Calculated long-term uplift rates are within ~15% of present-day measurements, while modelled rates of bedrock incision range from ~1 mm/yr for low gradient reaches between knickpoints to ~6–10 mm/yr close to retreating knickpoints, typical of observed rates in alpine settings. Together, our results reveal approximately 800 m of regional uplift, river incision, and hillslope erosion in the lower half of each tributary catchment since 0.7 Ma.

KEYWORDS

Glacial erosion; Fluvial erosion; River profile analysis; Landscape evolution; Quaternary; Swiss Alps

HIGHLIGHTS

- Fluvial knickpoints correlate across several major tributaries to the Rhone Valley.
- Profiles of these tributaries are inconsistent with modelled glacial erosion.
- Knickpoint distributions correspond to Late-Pleistocene glacial interval timings.
- Numerical models neglecting glacial erosion reproduce present-day river profiles.
- Fluvial and hillslope processes have dominated landscape evolution since ~0.7 Ma.

1. Introduction

Pervasive U-shaped, hanging, and overdeepened valleys attest to the importance of glacial erosion in shaping alpine topography. However, the debate as to whether these landforms are the result of cumulative erosion during cold climatic intervals (e.g. Penck and Brückner, 1909), or are the remnant of some early perturbation and have since been subjected to fluvial and subaerial erosion (e.g. Heim, 1885) remains one of the great discussions in Earth science (Fox et al., 2015; Korup and Schlunegger, 2007; Leith et al., 2014; Montgomery and Korup, 2010; Sternai et al., 2013; Valla et al., 2011; Valla et al., 2010). In the European Alps, there is still no radiometric, sedimentological, or remote sensing data to constrain the rate or magnitude of glacial or fluvial erosion during individual late-Pleistocene glacial – interglacial cycles, and as such, any information which sheds light on these important phases of climatically-driven landscape development can be invaluable to the community.

Insights into longer-term landscape evolution (encompassing several glacial – interglacial cycles) can be derived from a number of sources. In many cases, sediments overlying bedrock in overdeepened valleys have been found to pre-date the Last Glacial Maximum (LGM) (Preusser et al., 2010), and in locations such as Lake Geneva, the sometimes 1000 m deep valleys likely changed little during the last glacial period (Fiore et al., 2011). Sedimentological records are supported by recent evidence suggesting major valley incision and glacial sediment production in alpine settings occurred rapidly (within a few glacial cycles) (Shuster et al., 2011; Shuster et al., 2005; Sternai et al., 2013). In the European Alps, glacial valley formation may have occurred in response to an increase in global ice volumes following transition to ~100 ky climatic cycles at the mid-Pleistocene transition (MPT) during marine isotope stage (MIS) 22 (1250 – 700 ka BP). This is supported by observations of a rapid baselevel lowering from dated sediments in a cave system adjacent to the Aare Valley on the northern margin of the Swiss Alps (Häuselmann et al., 2007), a major one-off pulse of coarse glacially-derived sediment observed in the stratigraphy of the Po Plain to the south of the Alps (Muttoni et al., 2007), and a significant younging of thermochronometric ages in the Central Swiss Alps (Valla et al., 2012).

Although none of the above studies allow valley formation to be constrained to a single glaciation, Leith et al. (2014) recently put forward a new numerical model aimed at evaluating the development of bedrock fractures beneath a glacier incising into a V-shaped fluvial valley. Results suggest fracturing (a pre-requisite for glacial quarrying) initiates as glaciers erode into critically stressed bedrock in the valley floor, accelerates as the valley deepens (providing access to more highly stressed bedrock), and peaks with reducing confinement while glaciers thin. Importantly, a single cycle of strong erosion is expected to leave a layer of largely unfractured and de-stressed bedrock beneath the axis of the newly formed U-shaped valley. Continuing the model with a new phase of glaciation then suppresses fracturing, and likely prevents subsequent phases of strong glacial erosion (Leith et al., 2014). The Authors suggest this one-off positive feedback provided post-MPT glaciers a unique opportunity to dramatically alter the dominantly subaerial landscape of the early Pleistocene European Alps. Late Pleistocene glaciations may have then had limited impact on Alpine topography, while interglacial fluvial or hillslope processes instead drove valley formation (Leith et al., 2014).

Here, we test the implications of results presented in the above studies. We assume cold intervals following the MPT likely generated glacial conditions broadly similar to those of the LGM, when the ice surface within inner Alpine valleys lay between 2000 m and 3000 m a.s.l. (Bini et al., 2009). This is well above the estimated equilibrium line altitude for LGM glaciers (~1500 m a.s.l.), and as a result, glaciers were likely cold-based, and glacial erosion is expected to be relatively slow (e.g. Cuffey and Paterson, 2010) (see Section 1.2 for further details). Interglacial intervals following the MPT likely reduced any surviving glaciers to the highest elevations, while erosion and sediment transport were dominated by fluvial and hillslope processes. We first compare predicted patterns of glacial erosion to present-day topography in the region, highlighting inconsistencies that can be explained by a system dominated by interglacial fluvial and hillslope erosion. We then use a combination of LiDAR data and analysis of valley long- and cross-profiles to show that the location of steepened reaches within different sized tributaries, as well as both channel and hillslope form, can be explained with a simple fluvial erosion model and sympathetic linear adjustment of adjacent hillslope elevations since the MPT.

1.1. Setting

1.1.1. Regional Geology

Tributary channels in our study region of the southern Swiss Alps intersect the Rhone River as it flows across a thick sedimentary fill (Fig. 1). We investigate a subset of these channels, focusing on those occupying a relatively homogeneous tectonic block south of the Rhone that has most likely experienced monotonic uplift during repeated Pleistocene glacial – interglacial cycles (Serpelloni et al., 2013). Bedrock within this block belongs to a series of stacked nappes resulting from the north–south collision of the Apulian and European Plates between 65 Ma and 35 Ma. The subduction of intermediate terranes belonging to the Piemont-Liguria oceanic basin, Briançonnais microcontinent, Valais Ocean, and the European continental crust below the Adriatic plate led to the formation of a thick accretionary wedge, which was deformed and exhumed as the present-day Penninic nappes (Schmid et al., 1996). Our studied rivers lie almost entirely within the Siviez-Michabel nappe, a moderately (~30°) west–southwest dipping sequence of crystalline orthogneisses and paragneisses, mica-rich schists, and quartzites derived from the Briançonnais microcontinent (Escher et al., 1993) (Fig. 1a). Modern geodetic measurements indicate that differential rock uplift between the western extent of the study area and the outlet of Lake Geneva is approximately 1 mm/yr (Brockmann et al., 2012) (refer to Fig. S1 for a full uplift map), and geological evidence such as extreme topographic relief and rapid erosion rates (e.g. Fox et al., 2015; Steck and Hunziker, 1994; Valla et al., 2012; Wittmann et al., 2007) support similar rock uplift rates in the long-term. Although debate continues (Mey et al., 2016), recent geodynamic models indicate crustal rebound resulting from LGM deglaciation may not be a major contributor to the pattern of present-day uplift (Champagnac et al., 2009; Serpelloni et al., 2013), and the observed distribution may therefore be representative of average bedrock uplift conditions throughout the Late Pleistocene.

1.1.2. Tributary catchment morphology

Our investigated catchments share a common morphology: rivers sourced from headwater glaciers first flow through narrow, incised bedrock channels before traversing relatively short (~1–2 km) sediment-filled basins (Fig. 1b, profile a-a'). Most then pass through a short, steep bedrock reach (Fig. 2 section A) before traversing a broad alluvial plain extending several kilometres downstream (Fig. 2, section B). Large dip-slope bedrock landslides are common on the eastern side of the valleys in this region, while a distinctive glacial shoulder and U-shaped form is preserved on the western slopes (Fig. 1b, profile b-b',). The downstream limit of this alluvial plain (currently ~800 m above the Rhone River confluence) typically corresponds to a constriction of the valleys created by large landslides or debris fans (Fig. 2, transition from B to C), below which channel reaches are notably steeper and contain a series of steepened or convex channel sections. Rivers exhibit an overall linear profile as they pass across section C, although gradients decrease downstream of tributary intersections, a common observation in fluvial systems, as higher flows require lower gradients to erode or transport similar bed material. Frequent talus and debris flow fans within the upper half of section C likely reflect a sympathetic increase in hillslope activity, while exposed bedrock on the river bed in lower portions indicates fluvial incision is currently active.

The landscape transitions from a classical U-shaped form to a V-shaped cross-profile as we progress down through section C (Fig 1b & c). This transition is accompanied by a broad region of increased topographic roughness and mean hillslope gradients, which tapers upward from the full length of the section at the channel level to a point ~1500 m above the present-day channel (insets, Fig. 2). This morphology is indicative of relatively rapid hillslope erosion that stems from ongoing incision in the present-day channel. Narrow bedrock gorges with steep walls several 10's of meters high are common downstream of channel convexities in the lower half of section C (Fig. 2), suggesting fluvial processes have played an important role in shaping the landscape form. This is consistent with the findings of previous studies (Fox et al., 2015; Montgomery and Korup, 2010), which highlight the considerable time required (at minimum more than the current interglacial) to generate ~100 m deep inner gorges elsewhere in the Alps. Loose and fractured bedrock is ubiquitous on the walls of gorges in this lowermost region (near the transition of section C to D, e.g. Fig 3c & d), indicating erosion has

predominantly been driven by Holocene fluvial incision undercutting channel walls and subsequent rock slope failure, rather than the smooth sculpted forms typically associated with glacial erosion or sub-glacial meltwater (e.g. Jansen et al., 2014). The lowermost regions of larger catchments (Fig. 2, section D) display a distinct V-shaped cross-profile, with relatively planar soil-mantled hillslopes extending up to 1200 m above the river (Fig. 1b & c, Fig. 4). The valley floor in these regions is often narrow (<30 m wide) and sediment-filled, though geophysical surveys aimed at evaluating the depth to bedrock where the Borgne d'Arolla (Pfiffner et al., 1997) and Vispa (Burjánek et al., 2012) enter the Rhone Valley (Fig. 2) were unable to resolve the sedimentary cover, indicating the infill thickness is at most a few 10's of meters. The close proximity of bedrock to the present-day fluvial valley floor indicates neither tributary can be described as a hanging or overdeepened valley.

1.1.3. Sedimentology of the Rhone Valley

Seismic imaging and sedimentary evidence indicates that post-glacial infilling of the up to 1000 m deep glacial trough beneath the Rhone Valley was rapid (~60 mm/yr) and was largely completed by ~12 ka (Fig. S2a – c) (Finger and Weidmann, 1987; Hinderer, 2001; Pfiffner et al., 1997). Subsequent aggradation of alluvial sediments was limited to approximately 1.5 mm/yr, and while a strong anthropogenic increase to ~12 mm/yr is evident in the last 1000 yrs (Finger and Weidmann, 1987), present-day rates of ~1.4 mm/yr (Hinderer, 2001) are consistent with those prior to ~1 ka (Fig. S2d) (Hinderer, 2001). This late phase of anthropogenic sedimentation equates to approximately 25 ky of aggradation at normal Holocene rates, and the present-day sedimentary system may thus be more closely related to a mid- rather than early-interglacial landscape.

1.2. Predicted impact of glacial erosion

Results from two numerical models aimed at reproducing general patterns of glacial erosion in our study region (Herman et al., 2011; Sternai et al., 2013) provide a useful comparison between the observed morphology and that which may be expected for a glacial origin. Herman *et al.* (2011) and Sternai *et al.* (2013) incorporated subglacial hydrology with an oscillating climate representative of Mid- to Late Pleistocene glacial cycles to simulate bedrock erosion based on a basal sliding rule. The selected boundary conditions for both models are markedly different: Herman *et al.* (2011) do not include bedrock uplift, use a relatively high erosion constant, and simulate erosion from the present-day to 400 ky in the future. Sternai *et al.* (2013), on the other hand, assume a moderate tectonic uplift rate, a relatively low erosion constant, and simulate erosion from the MPT to the present-day. While the physics of each model are nearly identical, the absolute magnitudes of erosion predicted are not comparable. Sternai *et al.* (2013) predict a net elevation gain in tributaries as uplift exceeds erosion, while Herman *et al.* (2011) predict rapid erosion and exceptional relief development (Fig. 5a).

Assessing erosional potential allows us to compare key characteristics of the two models, despite large differences in the absolute magnitude of erosion and uplift. We define erosion potential as the net erosion at each node normalized by the total eroded volume along the axis of tributaries at the final model stage (Fig. 5b). This comparison illustrates that in most valleys, modelled glacial erosion potential is strongly linked to the drainage network topology, initially increasing with increasing catchment area before decreasing toward a point approximately 5 km from the junction with the Rhone Valley, presumably in response to a decrease in ice flow velocity. Similar effects can be observed where large tributaries merge (for example near the head of the Matter Vispa and at the confluence of the Matter and Saas Vispa), with all tributary valleys demonstrating a notable decrease in erosional potential near discrete steps in drainage area (Fig. 5b). Erosion potential immediately adjacent to the Rhone Valley in the two westernmost catchments (2 – 6 Borgne d'Arolla and 7 – 9 Navisence, Fig. 1) is very high in both models, reflecting a response of these catchments to high rates of modelled erosion in the adjacent Rhone Valley. For most reasonable initial topographies, these models therefore predict a tendency towards overdeepening of valley floors in the upper and middle reaches of the tributary catchments, shallowing of the longitudinal gradient in the mid- to lower reaches, and deepening adjacent to the Rhone Valley. Topography within the lower half of present-day valleys, however, does not reflect that predicted from these models. In particular:

- The convex break in longitudinal profiles dividing the broad alluvial plane (Fig. 2, section B) from a steep linear section of the valleys (section C) lies very close to the region of peak glacial erosion potential in each catchment. This *strong convexity* associated with an abrupt increase in channel steepness contrasts with the tendency of each model to *increase concavity* in response to greater glacial erosion near this location.
- The steep linear section of the valleys (section C) corresponds to a consistent downstream decrease in glacial erosion potential. As such, modelled valley profiles are concave along this reach. Aside from the Lower Navisence Valley (catchment 7), which crosses an active fault (see Fig. 10 for fault location), there is no field evidence for such concavity or erosional minima (e.g. overdeepened basins or bedrock promontories) at this point in any of our studied catchments.
- No catchments are significantly overdeepened with respect to the baselevel set by the Holocene sedimentary fill in the Rhone Valley. Large catchments contain shallow fill (e.g. Burjánek et al., 2012; Pfiffner et al., 1997), while smaller tributaries enter the Rhone Valley with either steep bedrock sections leading onto similarly graded alluvial fans (catchments 1, 16 – 18), or a 20 – 40 m high waterfall at the valley confluence (catchments 10 – 12).

We suggest these discrepancies reflect an inconsistency between assumptions in the glacial erosion models, and processes responsible for driving Pleistocene landscape evolution in this region.

1.3. Conceptual model of landscape evolution

We propose a conceptual model that provides an overview of anticipated landscape change following an initial period of intense mid-Pleistocene glacial erosion (Fig. 6a). We begin by considering the observed rapid sedimentation and ongoing uplift after the LGM to be a typical response of the Rhone Valley to major deglaciation (Fig. 6b). We then suggest that ongoing uplift during interglacial periods will lead to erosion of valley fill sediments as the Rhone River works to attain, and then maintain, a consistent profile in dynamic equilibrium with climate, catchment hydrology, sediment characteristics, and regional baselevel at Lake Geneva (Fig. 6c). Subsequent glaciations then remove the majority of sedimentary infill but do little to alter the broad form of the landscape, while uplift continues to raise bedrock (Fig. 6d). Depending on the degree of initial overdeepening, a number of glacial cycles may be required before bedrock on the floor of tributary valleys is uplifted above the interglacial sedimentary fill. At this stage, deglaciation will expose bedrock at tributary outlets (perhaps as a waterfall). This bedrock step will be steeper than the now uplifted fluvial section upstream, and erosion will cause it to gradually propagate into the catchment as a new knickpoint, before aggradation associated with early interglacial infilling of the Rhone buries the lower reaches of each channel (Fig. 6e & f). As the Rhone River attains dynamic equilibrium, uplift will cause the lower reaches of tributaries to begin incising, re-exposing the valley walls for the remainder of the interglacial. Subsequent glaciation then causes a dramatic slowing (or shutdown) of fluvial incision, allowing uplift to raise the elevation of bedrock channels relative to that of the interglacial valley fill (Fig. 6g). Assuming limited Late Pleistocene glacial erosion near the axes of tributary valleys, and invariant interglacial hydrological conditions, deglaciation and re-establishment of fluvial sediments within the Rhone Valley will then lead to the formation of a new bedrock step in each tributary close to the former bedrock–sediment interface (Fig. 6h). The height of these steps is determined by the duration of glaciation and the rate of bedrock uplift relative to baselevel. Renewed fluvial erosion during interglacial periods will then drive the migration of these steps upstream, and repeat glacial-interglacial cycles will thus produce a sequence of corresponding knickpoints within each catchment (Fig. 6h). Similar knickpoint sequences have been extensively used to infer tectonic histories from fluvial long-profiles (e.g. Roberts and White, 2010; Valla et al., 2010; Whipple and Tucker, 1999; Whittaker, 2012; Petit et al., 2017), however, the traditional assumption that glaciation always causes a significant modification to the longitudinal profile of alpine valleys has, to date, prevented similar analysis of glacial–interglacial events.

1.4. Predicted impact of interglacial erosion

The sequence described in our conceptual model provides a framework with which we can test for the development and preservation of interglacial erosional features through multiple glacial –

interglacial cycles. Where the evolution of the valley floor is dominated by fluvial erosion, river channels will adopt a profile closely related to changes in catchment hydrology, bedrock erodability, and tectonic uplift; while hillslopes may (in the simplest case) respond to fluvial incision through retrogressive erosion of frictional strength-limited slopes controlled by the progressive loss of bedrock cohesion (e.g. Burbank et al., 1996; Selby, 1982). These insights allow us to make a number of predictions regarding morphological attributes of valleys in our study region, the first two of which we have already discussed, while we refer to the remainder in Section 3 of this paper:

1. Longitudinal channel profiles should be consistent with that of a fluvial system, and demonstrate a reduction in gradient with increasing catchment area (see Section 1.1.2);
2. The most downstream elevations should approach that of the present-day Rhone Valley (see Section 1.1.2);
3. Channel profiles should be interspersed with similar knickpoints whose location and scale reflect rates of tectonic uplift, erosion, and the timing of MIS cold intervals;
4. Erosional efficiency should be similar for catchments throughout the study region;
5. Calculated uplift rates should not vary significantly from present-day measurements, and should be broadly consistent across the study area;
6. Hillslopes not affected by deep-seated mass wasting should demonstrate consistent gradients that project to intersections above the present-day valley floor;
7. Any remnants of pre-MPT fluvial topography (such as valley floors and convergent hillslopes) should intersect at an elevation around 750 m above the present-day Rhone Valley floor (allowing for relative uplift of 1 mm/yr and ~ 700 – 800 kyr duration).

2. Methods

We investigate morphological similarities between catchments in our study region using high resolution topographic data derived from a LiDAR DEM (swissALTI^{3D}, 2 m resolution, vertical accuracy of <0.5 m). We first test for correspondence between knickpoint sequences across catchments, comparing the pattern to the timing of cold MIS intervals using an integral analysis along each channel. Then, substituting catchment-specific constants derived from this analysis into a forward model of longitudinal channel evolution modulated by MIS timing, we test our conceptual model by comparing numerical results with present-day river profiles. Finally, we use intermediate stages of modelled channel evolution to highlight relict portions of cross-sectional valley form indicative of former interglacial channel elevations. We note that although our conceptual model provides the basis for interpretation of knickpoint locations and boundary conditions for simulated channel formation, it only affects our integral analysis insofar as it allows us to estimate an absolute timescale; the correlation of knickpoints between modelled and present-day catchments throughout the study region is otherwise independent.

2.1. Stream power model

Our conceptual model can be tested within the framework of the stream power model, which provides a simple description of how rivers evolve through time, accounting for upstream drainage area and the expectation that steepened reaches erode faster (Howard et al., 1994). The stream power model relates changes in channel elevation through time, dz/dt, to uplift rate, U, and erosion rate. The latter is parameterized as a function of upstream drainage area raised to a power (A^m), local along-channel slope (dz/dx), and erosional efficiency (K), which depends on mechanical and climatic factors. The model can be written as:

$$\frac{dz}{dt} = U - KA^m\left[\frac{dz}{dx}\right]^n \qquad (1)$$

where x and t are distance and time (Whipple and Tucker, 1999). In all but one catchment, we select exponents m and n to be 0.5 and 1, respectively (e.g. Whipple and Tucker, 1999). Exponents for the remaining catchment (rivers 2 – 6) are both (i.e. m and n) set to 1, partly to improve the correspondence of the modelled profile to that of the present-day, and partly to allow discussion of factors affecting these variables (and demonstrate the robustness of our analysis, as this choice does not significantly influence our conclusions (see Section B2 for commentary)).

2.2. Integral analysis

We first test for contemporaneous evolution of the tributary catchments by evaluating correspondence between convex long-profile segments and MIS timing using an integral approach, with modified χ or τ plots (Royden and Perron, 2013; Tucker and Whipple, 2002; Whittaker, 2012; Willett et al., 2014). This approach is based on Equation (1), an advection equation with kinematic wave speed $C = KA^m(dz/dx)^{n-1}$ (Whittaker, 2012), and we can therefore define the response time (τ) for knickpoints to propagate upstream from the baselevel x_0 to position x as (Royden and Perron, 2013; Willett et al., 2014):

$$\tau(x) = \int_{x_0}^{x_l} \frac{dx}{KA(x)^m} \qquad (2)$$

Characteristics of long profiles that are genetically linked will share a common τ value, despite being derived from catchments of different area. We compare present-day knickpoint locations to MIS stages and forward model results (discussed below) using a two-stage iterative search to automatically identify knickpoints, then assign each to a cold – warm MIS transition (see Appendix A for further details). While manually assigning each feature would likely provide more accurate results, we favour an automated approach for such a large area, as it ensures consistency and minimizes subjectivity.

2.3. Derivation of K, U, and x_0

We next use *a priori* knowledge of the glacial-interglacial marine isotope record to estimate the timing of knickpoint formation and derive values of U, K, and x_0 for each catchment (see Supplementary Table 1). These can be estimated by specifying the timing of knickpoint formation at two positions along each channel. Assuming knickpoints close to the floor of the Rhone Valley result from uplift and erosion since the onset of MIS 2 (the last glacial period), we can correlate intermediate knickpoints with consecutively older cold MIS stages to eventually determine the theoretical timing of formation for the uppermost knickpoint in the presumed fluvial portion of the valley (Fig. S3a). The mean uplift rate for each catchment is then given by the elevation difference between the two features, divided by the elapsed time (Δt) between deglaciation events ($U = (z_2 - z_1)/\Delta t$), while the erosional efficiency can be determined by dividing the elapsed interglacial time (Δt_{inter}) by the calculated difference in χ between the two locations ($K = \Delta t_{inter} /(\chi_2 - \chi_1)$). Although we assume uplift to be constant through time and therefore select total elapsed time for calculating uplift rate, fluvial incision is only assumed to be active during interglacial periods, and elapsed interglacial time is therefore appropriate for the erosional efficiency calculation. We assume the location of knickpoint formation (x_0) corresponds to the position at which $\tau = 0$ (i.e. the present-day) (Fig. S3c).

Although any two knickpoints can be chosen for this process, we select the midpoint of the lowermost and uppermost features that can confidently be identified in order to minimize numerical errors. If one or more downstream knickpoint is obscured by external influences (e.g. debris fans or landslides), comparing the remaining intermediate knickpoint locations to glacial events (marked by breaks in elapsed interglacial time) or elevation above the Rhone plain (as uplift rate varies gradually across the region), provides verification of the selected knickpoint ages. As the specification of upper and lower knickpoints directly determines U, K, and x_0 for each tributary, an error in the selection of interval will become apparent when these parameters are compared across tributaries.

2.4. Forward model

To verify results from our integral approach, address effects of knickpoint diffusion, check for geomorphic complexity in present-day profiles (e.g. mass movements, fault displacement, drainage divide migration), and evaluate intermediate stages of incision and their effects on hillslope morphology, we use parameters derived from our initial analysis to simulate development of longitudinal tributary valley profiles.

We solve the modified stream power equation using an explicit, upwind finite-difference method. Our initial channel profile, reflecting that of the valley floor following U-shaped valley incision, is largely unconstrained and we start our models with a low-gradient linear profile sloping down to the valley confluence at 0.6°. This is a simplified representation of a low-gradient alluvial valley floor, through which uplift and fluvial incision gradually expose underlying bedrock. This assumption has little effect on our final results, as the evolution of the fluvial profile with a response time less than $\tau(x)$, for example, depends only on the rock uplift history between 0 and $\tau(x)$ (Royden and Perron, 2013), and as long as the initial bedrock topography does not have significant overdeepenings, its form will not influence the propagating knickpoints. Values of U, K, and drainage area at x_0 are derived from our identification of upper and lower fluvial knickpoints, and time steps are chosen to ensure stability and accuracy. Knickpoint formation is simulated as an instantaneous pulse of uplift calculated from the duration and rate of uplift during glacial periods, and knickpoints are formed at a position corresponding to $\tau = 0$. We simulate interglacial sedimentation, uplift and incision at the Rhone Valley by raising a 0.6° sloping sedimentary fill (which prevents erosion) at a rate of 1.5 mm/yr above the calculated uplift rate for 25 ky, while increasing the bedrock channel elevations at the calculated uplift rate. After 25 ky, we hold the absolute elevation of sediment cover constant, while continuing tectonic uplift elevates the bedrock channel. The final interglacial cycle (to the present-day) includes an increase in sedimentation rate to 12 mm/yr for the last 1 ky to account for anthropogenic change (see Section 1.1.3). We do not include complex geomorphic processes mentioned above, such that model results reflect an idealized uplift-erosion history, and τ plots can be compared to those derived from longitudinal profiles to evaluate the effects of external factors (see Supplementary Table 2 for all model variables).

As knickpoints in the measured river channels appear increasingly broad and less angular with increasing distance from the Rhone, we use a modified version of equation (2) that incorporates a diffusion term $\kappa d^2z/dx^2$, where κ (assumed to be 5 mm^2/yr) is the channel diffusivity. This reflects a common observation for knickpoint sequences in alluvial channels and may be related to accelerated erosion at the knickpoint crest. Alternative explanations for the observed diffuse knickpoints may involve variations in the initial geometry (which is unlikely to have been angular as simulated, see catchments 11 & 12, Fig S3b), localized sub-glacial erosion, or increased erodibility at knickpoint crests. Incorporating a diffusion term offers the simplest approximation. Although this does not alter the position of modelled knickpoints, it does reduce the steepness of these features as they migrate upstream, supporting our observations from LiDAR data.

Supplementary Table 3 contains inputs (K, U, simulated number of warm MIS intervals, and initial knickpoint locations) and corresponding predicted knickpoint locations from our forward models.

2.5. Correlation with hillslope morphology

Forward models of longitudinal channel profile development provide a useful opportunity to evaluate the connection between transient knickpoint migration and the erosion of adjacent hillslopes. Although a detailed evaluation of catchment morphology is beyond the scope of this study, we use profiles derived from end-of-interglacial model stages (when incision rates are at a minimum) as a reference to search for evidence of hillslope morphologies associated with relatively stable catchment conditions. We do this by applying the simple concept of strength-equilibrium hillslopes (Selby, 1982), in which stable slope angles are assumed to be defined by the strength of underlying bedrock, and simply projecting lines of constant gradient (defined by existing local topography) upslope from the modelled end-of-interglacial channel profiles.

3. Results and Discussion

3.1. Catchment characteristics

The mid- to lower reaches of our studied rivers (Section C, Fig. 2) display an overall linear profile, which consistently decreases in gradient at major confluences and is overprinted by a series of steepened, convex knickpoints (e.g Fig. 7c & d, S3a, & B1e). The uppermost knickpoint in each catchment corresponds to the downstream limit of the broad alluvial plain (Section B) and marks the lower extent of our presumed relict glacial topography. As the local ice surface lay between 1000 m and 1500 m above the LGM ELA in these areas (Bini et al., 2009), numerical models (Herman et al., 2011; Sternai et al., 2013) and morphological analyses (Hergarten et al., 2010; Robl et al., 2015) indicate this plane is unlikely to represent the effects of a 'glacial buzzsaw' (e.g. Egholm et al., 2009; Koppes et al., 2015), where overdeepening is due to a peak in glacial activity about the LGM ELA.

3.2. Comparison of modelled and observed valley characteristics

3.2.1. Knickpoint distribution

Tributaries in our study area typically display between four and six knickpoints demonstrating similar curvature and relative elevations (prediction no. 3, see Section 1.4). This pattern is illustrated for two large catchments on either side of the study region in Figure 7a - f. Based on our estimation of uppermost MIS ages, we expect in total 70 glacial – interglacial transition knickpoints across all channels. Results of our iterative search (see Appendix A) indicate that 57 convex sections identified in our LiDAR data correspond to the expected location of knickpoints, while in comparison, diffusion of the uppermost knickpoints only allowed us to identify 54 knickpoints in the modelled profiles (Fig. 8, Fig. S1a). The position of knickpoints correlates favourably with results from our climatically-modulated forward models, with a standard deviation between predicted and observed knickpoint ages of 9.6 kyr (inset, Fig. 8a), significantly less than the ~42 kyr duration of interglacial periods (Lisiecki and Raymo, 2005). We observe little to no correlation between knickpoint locations and variations in either lithology or stream power due to the confluence of tributary channels (cf. Fig. 1a & Fig. S1a, Fig. S3a). Identified convex reaches are overlain on the observed and modelled τ profiles in Fig. A2. Note that the relatively short duration glacial at MIS 14 and interglacial at MIS 17 produce subtle, diffuse MIS 14 & 16 knickpoints in the final stage of models covering this period. These were not identified as convex channel sections using search parameters derived from LiDAR data, however, the knickpoint formed at MIS 18 is identified in both LiDAR data and our forward model results. Smaller catchments with less obvious glacial imprint (e.g. Val Nendaz (1) and Dixence (4)) display profiles consistent with between seven and nine cycles of knickpoint formation and interglacial erosion (see Fig. S1), supporting evidence for major valley incision prior to MIS 18 (760 ka BP) (e.g. Häuselmann et al., 2007).

3.2.2. Longitudinal profiles

We find very good agreement between profiles derived from LiDAR data and our forward model results, with a mean residual error of just 26.3 m over the ~100 km of channel reaches analysed (providing further support to prediction no. 1, see Section 1.4). This is demonstrated for catchments 6 (Borgne d'Arolla) and 15 (Saas Vispa) in Figure 7, where almost all major morphological features are reproduced in the modelled profiles. Comparisons for the remaining catchments can be observed in Fig. S3c & d, B1, and B2. Calculated uplift rates are ~1.5 mm/yr, and vary gradually across the study region (prediction no. 4). These are slightly higher than present-day measurements of ~1.25 mm/yr, while interestingly, the spatial trend in calculated rates bears some similarity to the interpolated uplift map of Brockmann et al. (2012) (see Fig. S1b). In line with prediction no. 5, calculated mean incision rates vary between ~1 mm/yr, for reaches between knickpoints, and ~6 – 10 mm/yr close to retreating knickpoints, consistent with values determined from similar tectonically active regions (Koppes and Montgomery, 2009).

Our results demonstrate a strong sensitivity to the assigned upper knickpoint age, and knickpoint distributions, uplift rates, incision rates, and model profiles rapidly diverge from the present-day values

when an alternative selection is made. If upper knickpoints are assigned an age corresponding to the next oldest warm MIS, the mean residual error increases to 84 m as the most upstream knickpoint develops slightly lower and further upstream than observed, while perturbations in the channel are smoothed and channel concavity increases. If instead we assume the most upstream knickpoints are younger, the mean error increases to 223 m as the rate of uplift and incision during interglacial stages increases markedly (exceeding typical Alpine rates), while upstream propagation of knickpoints is limited and the fluvial portion of catchments tends to be shorter and steeper than evident in our study region. Excluding uplift during glacial stages has a similar effect, as uplift and incision during interglacial stages must almost double. Supplementary model runs in which sedimentation was not included produced results nearly identical to those presented here, while runs in which sedimentation was allowed to continue throughout each interglacial (i.e. for > 40 ky) led to preservation of larger, more angular steps than observed in the landscape today. See Appendix B for additional detail on the model performance.

3.2.3. Cross-sectional valley form

Although both our inverse analysis and forward models are independent of cross-valley profiles, we also find distinct breaks in hillslope angles, above which linear profiles project toward modelled end-of-interglacial channel positions (Fig. 4 & 9). This finding is consistent with the expected morphology of hillslopes formed in response to periods of relatively stable baselevel, followed by rapid erosional events associated with either knickpoint retreat or cyclic variations in stream power (prediction no. 6). Downstream of each knickpoint, we commonly find either narrow inner gorges up to 100 m deep (Fig. 2, Fig. 3), or a slight terracing and/or steepening of the valley sides (Fig. 4a – c), indicating adjacent hillslopes have been affected by headward propagation of knickpoints following a spatial or temporal change in erosion rates. A distinct break in the cross-profile of all Rhone Valley tributaries is also evident where broad upper slopes with rugged topography transition to narrow, linear 'V'-shaped valleys at elevations below approximately 1200 –1600 m a.s.l. (prediction no. 7, Fig. 4 & 9). Extrapolated upper slopes commonly converge toward the initial elevation of our modelled rivers (representing the pre-fluvial incision valley floor, see Fig. 1c), suggesting that valley-scale topography has evolved in response to falling fluvial baselevel, and hinting at elements of a remnant landscape preserved above the current extent of V-shaped sections. Together, these results support our interpretation of climatically-modulated, fluvially-driven Late-Pleistocene landscape evolution for which both channel and valley morphologies have been preserved through several glaciations.

3.3. Comparison with glacial erosion models

Our model results indicate that fluvial incision has propagated approximately half-way into each of the Rhone tributary catchments, and our models (which treat glaciation simply as a period of zero erosion at the valley axis) accurately reproduce the long profiles in this portion of the valleys (Fig. 10a). Upstream, in areas unaffected by propagating fluvial incision, we find a similarly good match between the valley longitudinal profile and adjusted profiles derived from those presented as a 'present-day' stage considering primarily glacial erosion by Sternai et al. (2013) (Fig. 10b). For the latter, we vertically shifted and scaled the results derived for each catchment to minimize residuals between the observed and calculated profiles in the 'glacial' sections. While this will require more rigorous analysis in the future, our adjustment mimics a change in uplift rate, initial elevation, and erosion coefficient, and as such is therefore reasonably faithful to the original model. Our 'best of both worlds' hybrid valley profiles can thus be regarded as demonstrating the relative effects of fluvial and glacial erosion on different sections of the longitudinal profiles of these tributary Alpine valleys since the MPT.

4. Conclusions

Our results suggest that large-scale Pleistocene landscape evolution in the central European Alps has been driven by tectonic uplift and interglacial fluvial erosion following a period of rapid glacial valley carving prior to MIS 18. We identify up to 800 m of fluvial incision in the lower reaches of our studied tributary valleys, and find that signals of transient fluvial erosion have propagated roughly half-way through each catchment (depending on erodibility, geometry, etc.). Overall valley morphologies

are consistent with this result, and characteristic stepped, V-shaped cross-profiles in mid- to lower reaches suggest the landscape has progressed toward the formation of strength-equilibrium slopes in response to fluvial incision through multiple interglacial cycles. In agreement with the early conclusions of Heim (1885), we find that topographic evolution through glacial erosion during cold intervals lags far behind the combined effects of interglacial fluvial incision, subaerial hillslope erosion, and long-term tectonic uplift. The onset of glaciation therefore causes a relative still stand in valley formation.

Identifying key processes responsible for the formation of major Alpine valleys in our study region provides new insights into the absolute age and rates of topographic development. Further validation in the form of absolute dating and additional morphological analysis in similar (e.g. the Southern European Alps) and contrasting (e.g. the Southern Alps of New Zealand) mountain ranges will provide important constraints on the range of environments over which our results are applicable. It is important to note, however, that applying existing techniques to date erosional features formed after the MPT but prior to the LGM in this region is technically challenging, as erosion rates are too low to be detected with low-temperature thermochronometers (that could be used to constrain topographic changes over the last ~0.5 - 1 My, cf. Valla et al., 2012), while as little as 3 m of erosion during the last glacial cycle will remove almost all cosmogenic isotopes from surface bedrock (Duhnforth et al., 2010). Addressing these limitations will facilitate the application of insights derived from long-term erosional histories to improved understanding of alpine tectonics, mechanistic models of erosional processes, and awareness of associated geohazards.

Supplementary Materials

Table S1

Table S2

Table S3

Appendix A: Identification and classification of knickpoints

We calculate τ / (Z/U) profile gradient and convexity using a sliding window of 30 kyr, while gradient anomalies are calculated by comparing this value to the mean gradient across 300 kyr. We then use a two-stage iterative search to objectively classify convex channel anomalies ($f''(\tau)$ in τ - z space) as knickpoints, then correlate these features with predicted MIS transitions. Parameters derived from the observed channel profile search are then used to identify knickpoints in the modelled channels. We use published MIS intervals (Lisiecki and Raymo, 2005), rather than selected $\delta^{18}O$ thresholds, in order to reduce assumptions and simplify our analysis. We note this simplification is unlikely to be the largest source of uncertainty in our analysis.

Our search progresses from the lowest point of a channel to the head, during which convex channel sections are assigned to a glacial - interglacial MIS transition based on the closest match between the calculated τ (plus a factor to account for diffusion - see below). When a convex section upstream is found to be a closer match to the transition age, the previously assigned section is unassigned and recorded as a false positive (later counting against the accuracy of identification). This ensures the search doesn't 'refine' the match, so much as exclude obviously incorrect points. In the first search stage we allow the cutoff threshold for convexity anomalies ($f''(\tau)_c$) to vary from the mean of each profile ($\overline{f''(\tau)}$) by:

$$f''(\tau)_c = \overline{f''(\tau)} + \alpha\sigma \qquad \text{(A.1)}$$

where σ is the standard deviation of $f''(\tau)$ and α, the cutoff threshold, is varied between 0.25 and 1.25. As we assume the identified convex channel anomalies relate to knickpoint crests, which have diffused upstream over time, we allow τ values for MIS transitions to vary by:

$$\tau_d = \beta\tau_u \tag{A.2}$$

where τ_u is the duration of the next oldest warm interval and β is a factor that ranges between -0.05 and 0.55. For example, if a convex section with a τ value of 250 kyr is identified upstream of the position predicted for MIS 12 (τ = 230 kyr, τ_u = 55 kyr), it will be associated with the MIS 12/11 transition for β values less than 0.15, and MIS 14/13 for values above.

We identify an optimal convexity threshold, which maximizes the accuracy of knickpoint identification (evaluated from a balanced F0.5-score ($F_{0.5}$)) while minimizing the dispersion of identified features (characterized by the standard deviation of knickpoints from the predicted transition age (σ)). The balanced F0.5-score provides a measure of accuracy for a binary test as defined by the weighted average of precision and recall, in our case:

$$F_{0.5} = (1+0.5^2)\frac{\frac{p_t}{d_t}\times\frac{p_f}{d_t}}{0.5^2\times(\frac{p_t}{d_t}+\frac{p_f}{d_t})} \tag{A.3}$$

where p_t is the total number of true positives, p_f is the total number of false positives, and d_t is the predicted number of knickpoints within the investigated channels determined from the distribution of τ values in the dataset with respect to predicted MIS transition ages (defined by $\tau + \tau_d$). We evaluate equivalent variations in the F0.5-score and dispersion by calculating the product of the reciprocal of the normalized standard deviation (σ_{norm}) and normalized F0.5-score ($F_{0.5norm}$). We then identify the optimal combination of α and β by searching for that which maximizes the signal from our observed channel profiles (S), as defined by the two scores, i.e.:

$$F_{0.5norm} = \frac{F_{0.5} - \min(F_{0.5})}{\max(F_{0.5}) - \min(F_{0.5})} \tag{A.4}$$

$$\sigma_{norm} = \frac{\sigma - \min(\sigma)}{\max(\sigma) - \min(\sigma)} \tag{A.5}$$

$$S = F_{0.5norn} \times (1 - \sigma_{norm}) \tag{A.6}$$

The F0.5-score, standard deviation, and optimized solutions for the full parameter space are presented in Fig. A1a – c. We use these same parameters to classify knickpoints in both modelled and observed channels (Fig. A2).

Appendix B: Performance of the stream power model

B1. Apparent variations in erosional efficiency

An interesting result of our analysis is that K is not uniform across the study area. This erodibility parameter is frequently assumed to be constant, although few studies of river profile evolution make *a priori* assumptions regarding the magnitude and timing of knickpoint formation for individual rivers. Variations in K indicate that precipitation, tooling efficiency, bedrock strength, or *in situ* stress conditions vary across a given region. In our case, this may be partly explained by drainage divide migration, as knickpoint migration rate is a function of upstream drainage area, and changes in drainage area therefore lead to changes in migration rate over time. Because we have used the present day drainage network to calculate drainage areas, we have not explicitly accounted for drainage divide migration. However, as τ is a function of drainage area (see equation 2), this change in drainage area is mapped into a change in K. This is particularly evident where baselevel fall in the larger of two adjacent catchments has propagated planar hillslopes up to the ridge crest, creating asymmetric drainage divides (Fig. S1a). We note that agreement of knickpoints is weaker in smaller catchments where absolute changes in area have a greater effect on the overall catchment geometry, although we also observe generally higher K values in catchments experiencing higher rates of uplift (Fig. B3). Spatial and temporal controls on K therefore require further investigation.

B2. Variation in m and n

Supplementing our integral approach with forward models initialized using conditions that reflect an emerging glacial valley floor allows us to evaluate the selection of m and n values for the two approaches. In general, lower values of m tend to increase the concavity of the τ profile, as demonstrated for the Dixence and Borgne d'Arolla channels (2 – 6, Fig. B1c & d), while higher values of n tend to increase the incision rate at low gradients, and therefore decrease the steepness of modelled channels. Although we could reproduce the τ profiles for different combinations of m and n using a spatially variable initial topography (above the sedimentary fill level) and/or erodibility, these are likely to be somewhat contrived, and may bear no resemblance to the landscape itself.

Spatial and temporal variability in climatic and geomorphologic factors can also affect the relationship between stream power, catchment area, and channel slope, complicating assessment of m and n values. With selected values of $m = 0.5$ and $n = 1$, we are able to generate a reasonable fit between modelled and measured river profiles in all channels, although we find a better correlation of knickpoint locations with MIS timing and observed channel morphology assuming $m = 1$ in the channels of the Dixence and Borgne d'Arolla catchment (Fig. B1e). We suggest this represents a deficiency in the long-term relationship between catchment area and precipitation, rather than a problem with the common assumption that the scaling parameter $m = 0.5$. In particular, our study region presently experiences a strong gradient in annual precipitation from north to south, leading to a northward decrease in equivalent stream power per unit area. In addition, incision at the downstream end of the catchments has caused drainage divides to migrate into the neighbouring catchments (see Fig. S1). Both of these effects will tend to skew long-term calculations based on current catchment geometries, inducing an apparent downstream decrease in stream power per unit area, which can be roughly offset by increasing the value of m.

B3. Rock slope instability

Landslides appear to decrease local incision rates. Notable perturbations associated with large landslides are evident in the longitudinal profile of the Matter Vispa (catchment 14), where sediment contributions from the Graechen (~7000 m^3/yr) and Randa (>30 Mm^3 since 10 ka) landslides appear to have protected the bed from incision (Fig. B2a – c). Our modelled river channel adjacent to, and upstream of, the large creeping landslide at Graechen is almost 100 m below that of the observed channel, and although the knickpoint at the toe of the landslide lies in bedrock and is close to the predicted knickpoint location, the next upstream knickpoint is currently mantled in sediment (Fig. B2). Forward model results suggest the Graechen landslide may have initiated as a knickpoint formed during MIS 8 and progressed past the toe of the slope during MIS 5, slowing the propagation of downstream knickpoints but leaving those upstream unaffected (Fig. B2). The farthest upstream knickpoint in the Matter Valley (end MIS 12) coincides with the large talus deposit beneath the Randa rock slide. This debris cover likely masks the location of the underlying knickpoint, although bedrock outcropping in the channel 3 km upstream supports our interpretation of a bedrock knickpoint in this area.

B4. Glacial overdeepening of valley floors

As each profile records changes in uplift and stream power since first exposure of bedrock on the valley floor, the signal in formerly overdeepened valleys may include a time lag associated with uplift required to elevate bedrock above sedimentary fill. Based on calculated mean uplift rates and an estimated 300 ky lag time between MIS 19 – 12, initial overdeepening of the two largest catchments (Val Borgne (2 – 6) and the Vispertal (13 – 15), $U \approx 2.0$ & 1.4 mm/yr, respectively) may have exceeded 400 m. We note that we are unable to reproduce observed profiles without including initiation of incision prior to MIS 16 in our forward models.

B5. Evidence for ice-free conditions during MIS 3

Our results support the hypothesis that the inner Swiss Alps were largely ice-free during MIS 3 (see Döppes et al., 2011), as prominent ~60 m high knickpoints (expected close to the Rhone Valley if full glacial conditions persisted from MIS 4 – 2) are commonly not present. Smaller catchments in the north of the region (e.g. 1, 7 – 9, and 10) do, however, display such features, and we propose a combination of drainage capture by larger catchments, increasing orographically-derived precipitation gradients (resulting from ~1 km of bedrock uplift since MIS 18), and/or incomplete sediment evacuation during the relatively short (~17 ky) MIS 3 interglacial, likely reduced the local efficacy of fluvial erosion (as predicted by numerical models in which sedimentation was allowed to continue throughout interglacials – see Section 3.2.2).

Acknowledgments

We thank S. Loew and M. Krautblatter for supporting this study; J. Brosda for technical assistance; F. Herman and P. Sternai for glacial erosion model outputs; M. Spagnolo, L. Goren, K. Whipple, S. Brocklehurst, J. Jansen, and J. Webb for critical review and discussion; and E. Brockmann and A. Schlatter from the Swiss Federal Office for Topography swisstopo for provision of present-day uplift data. This study was partially supported by ETH Research grant ETH-29 09-2. MF was supported by NERC (NE/N015479/1).

Figures and Tables

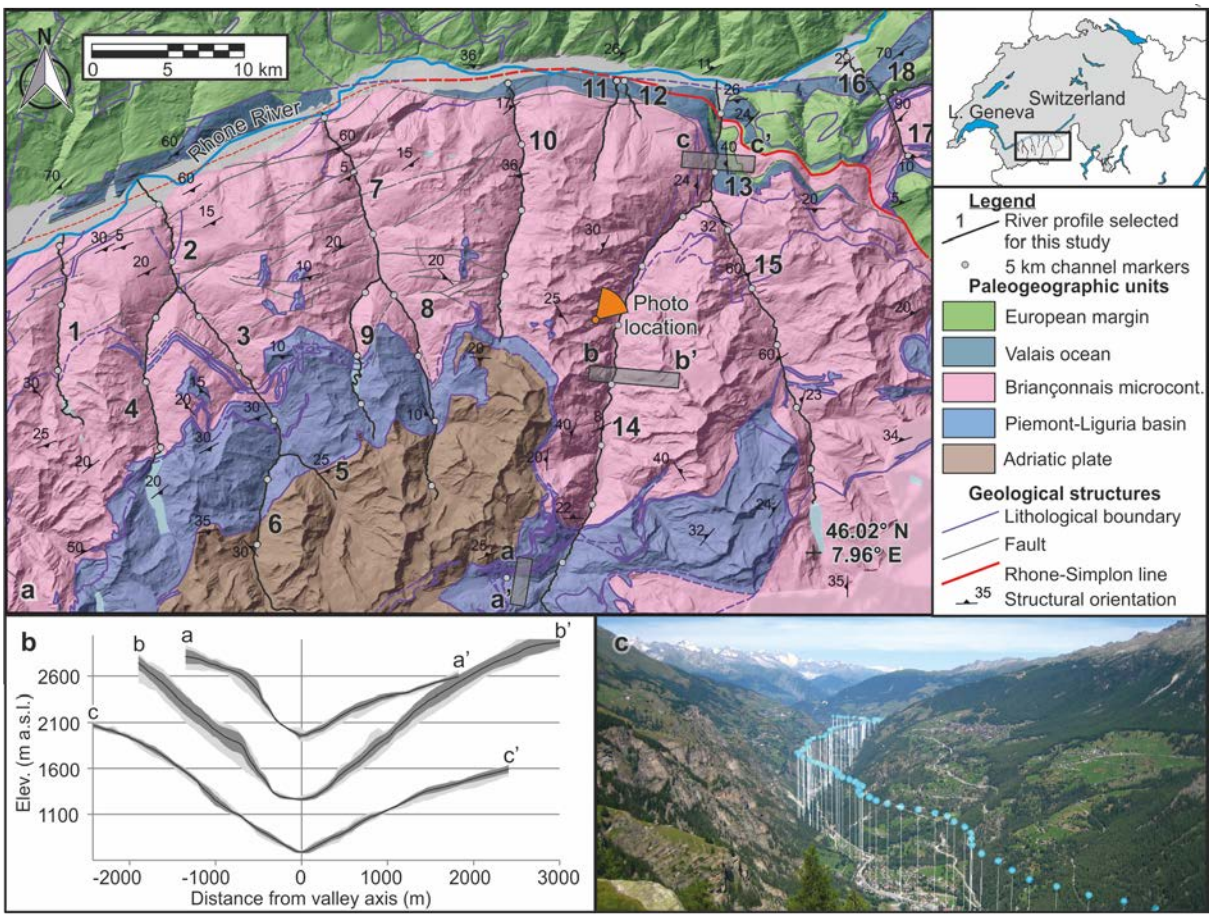

Fig. 1. a) Geological map of study area and selected river channels (after Spicher, 2005). Listed rivers are: 1. La Printse, 2. Lower Borgne, 3. Upper Borgne, 4. Dixence, 5. Borgne d'Ferpècle, 6. Borgne d'Arolla, 7. Lower Navisence, 8. Upper Navisence, 9. Gougra, 10. Turtmänna, 11. Milibach, 12. Löübbach, 13. Vispa, 14. Matter Vispa, 15. Saas Vispa, 16. Lower Saltina, 17. Taferna, and 18. Upper Saltina. **b**) Swath profiles of glacial (a-a'), transitional (b-b'), and fluvial (c-c') valley sections. Black lines describe the mean elevation, while grey shades indicate 1 and 2 standard deviations. **c**) Photograph of the lower Matter Valley indicating the calculated elevation of the initial fluvial channel (MIS 13). Prominent ridges in the fore- to middle-ground converge toward the initial channel elevation, and are characteristic of surfaces that may reflect a post-glacial, pre-uplift topography in the study region.

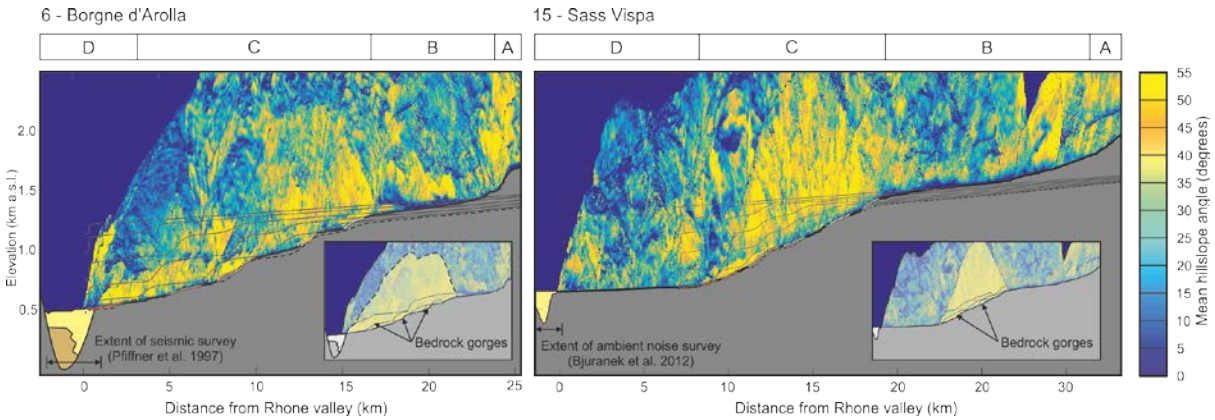

Fig. 2 Hillslope steepness maps for the Borgne D'Arolla and Saas Vispa. Sections A – D represent common geomorphological domains evident throughout the study region. Slope gradients are calculated as the mean of slopes either side of the channel. Subsurface data are derived from geophysical surveys (see Section 1.1.2). Profile lines above the present-day channels reflect modelled post-glacial channel profiles (see Section 3.2.2). Insets highlight regions of increased mean slope gradient and dissection thought to reflect the hillslope response to interglacial incision in section C.

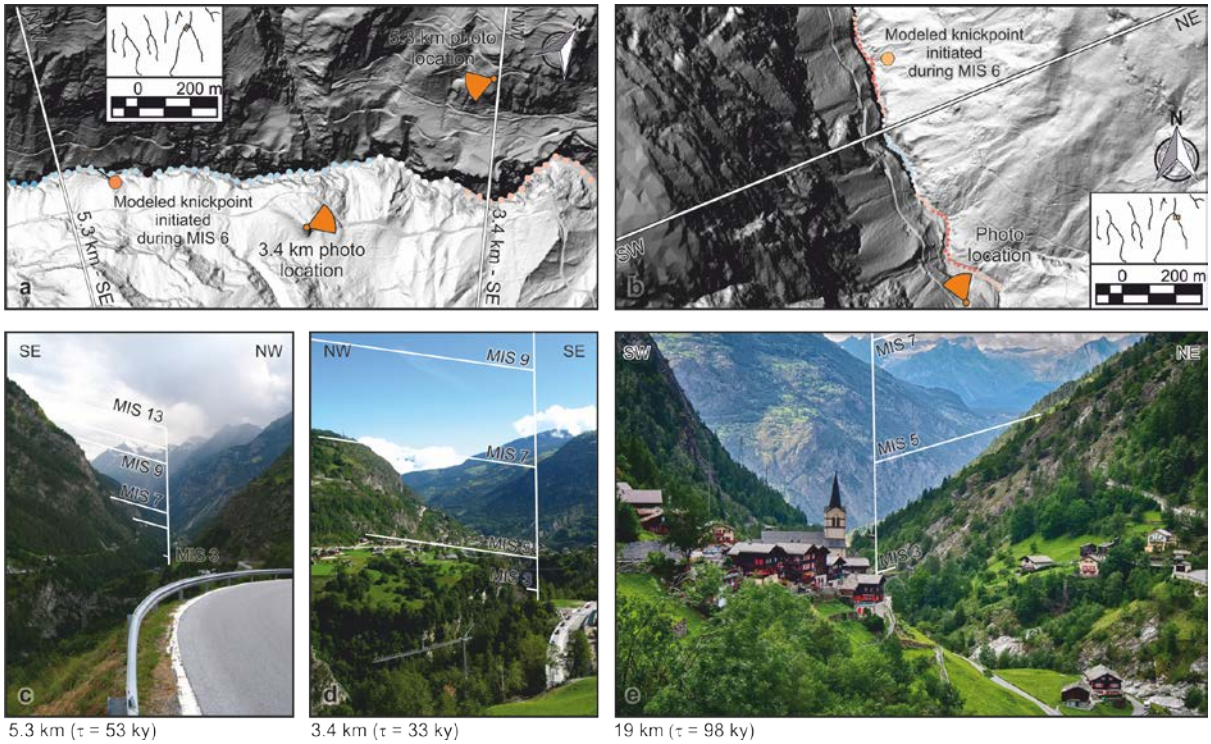

Fig. 3 Matter and Saas Vispa topography at the location of approximately 600 m of modelled fluvial incision. Modelled end-of-interglacial channel elevations are superimposed for reference. **a & b**) Shaded relief image and τ profile curvature (red is convex, blue is concave, see Fig. S1 for full colour scale). Map locations with respect to rivers in the study region is illustrated in the inset. **c**) Photograph illustrating V-shaped valley topography at the 5.3 km cross-section. Modelled end-of-interglacial channel elevations are superimposed for reference. **d**) Photograph illustrating a terrace corresponding to MIS 5 at the 3.4 km cross-section location. **e**) Photograph illustrating V-shaped form at the cross-section location, as well as the bedrock river channel seen plunging steeply down slope in the lower-right of the image.

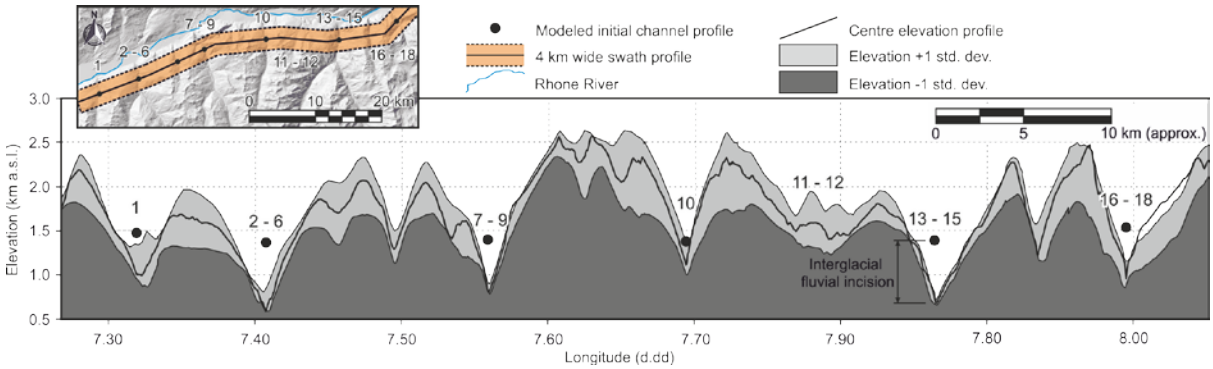

Fig 4 Swath profile (4 km wide) across tributaries south of the Rhone Valley. Initial channel elevations for forward models are superimposed on the profile where they cross the swath centreline. Topography between the modelled profile elevations and valley floors is characteristically 'V' shaped, supporting model predictions of fluvially-driven topographic change in this region. Highlighted is nearly 800 m of modelled fluvial incision in the Vispa valley (13-15). Vertical exaggeration is 10X.

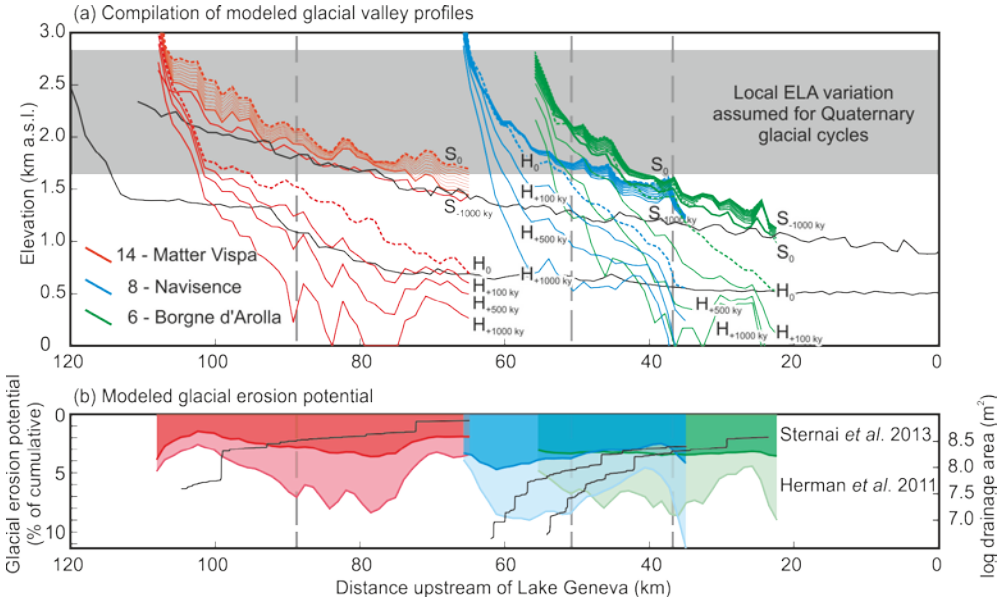

Fig 5 Comparison of calculated stages of glacial erosion for three tributaries in the study region (after Herman et al., 2011; Sternai et al., 2013). a) Longitudinal profiles for valleys at the end of simulated glacial stages. S_0 and H_0 refer to the present-day elevation of the axis in Sternai et al. (2013) and Herman et al. (2011), respectively. S-1000 ky and H+1000 ky then refer to the profile of the modelled position of the valley floor 1 My in the past, and future, respectively. Black lines represent the profile of the Rhone Valley in the initial stage of both models. Vertical light grey lines represent the boundary between sections B and C in each catchment (considered to be the upstream extent of Pleistocene fluvial erosion). **b**) Normalized mean erosion potential for each of the model runs. Results are stacked in order to emphasise the effect of the shared valley network topology on model results. Solid black lines depict drainage area in each tributary.

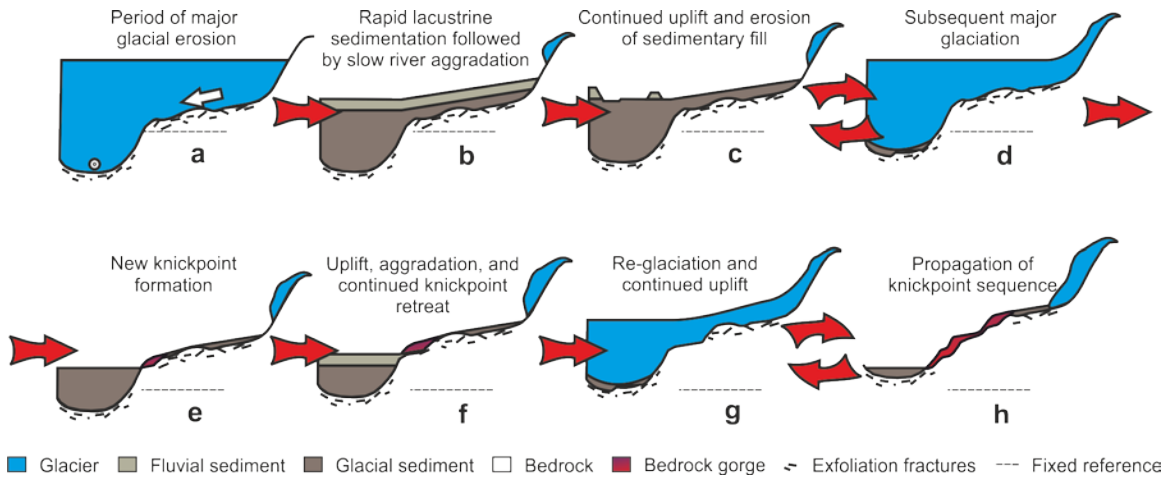

Fig 6 Conceptual model of knickpoint development. A) Glaciers carve deep tributary and trunk valleys. **b**) With deglaciation these valleys rapidly fill with sediment. **c**) Erosion of valley fill as aggradation and tectonic uplift cause the Rhone River to achieve dynamic equilibrium with respect to interglacial catchment hydrology and local baselevel at Lake Geneva. This causes an apparent increase in the bedrock elevation relative to alluvial valley fill. **d**) Subsequent glaciation removes most valley sediments, while continued uplift increases the elevation of bedrock beneath a protective ice cover. **e**) A return to interglacial conditions causes reestablishment of the alluvial valley floor, while bedrock uplift during the glacial period now exposes a bedrock step at the tributary outlet. **f**) Fluvial incision causes the bedrock step to migrate upstream, while tectonic uplift continues relative to Lake Geneva. **g**) Subsequent glaciation and rock uplift with limited bedrock erosion. The height of the bedrock step during the next interglacial is determined by the duration of glaciation and mean uplift rate. **h**) New interglacial conditions rejuvenate fluvial incision and knickpoint retreat.

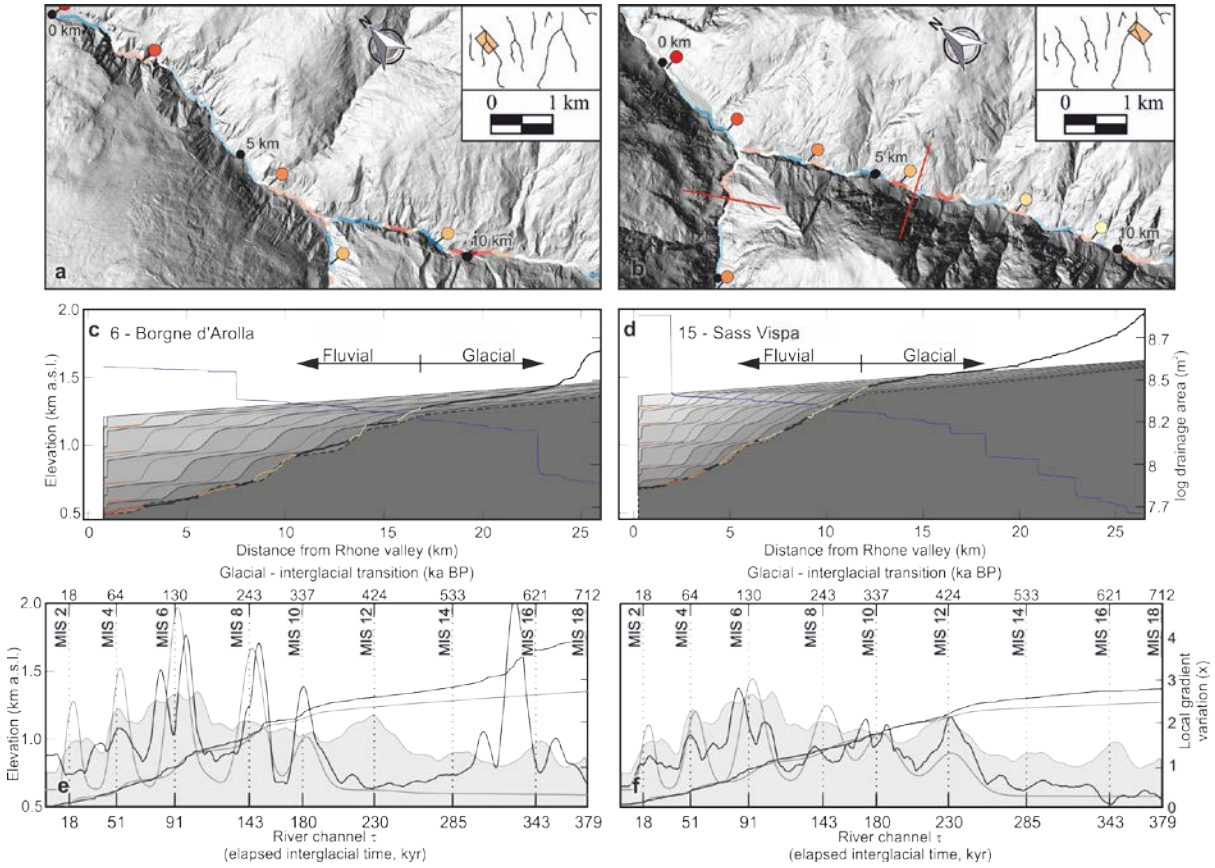

Fig 7 Comparison of simulated and observed channel profiles in the Borgne d'Arolla and Saas Vispa catchments (separated by ~35 km). a) & **b**) LiDAR-derived hillshade images of the lower catchments. Channel colouring indicates calculated convexity (see Fig. S1 for colour scale), while circular markers indicate modelled τ values representing glacial intervals associated with knickpoint generation. Red lines denote the position of cross-sections presented in Fig. 3 & 4 **c** & **d**) Forward model stages calculated at each glacial – interglacial transition, and 20 ky intervals thereafter. Red lines denote sedimentary fill, while dashed profiles indicate the modelled present-day profile. Blue lines indicate catchment area, while coloured sections on the observed profiles highlight interpreted knickpoint locations. **e** & **f**) τ plots of observed (black) and modelled (grey) present-day channel profiles. Local gradient variations for each are also indicated, while the shaded background presents the mean gradient variation for all channels in our study region.

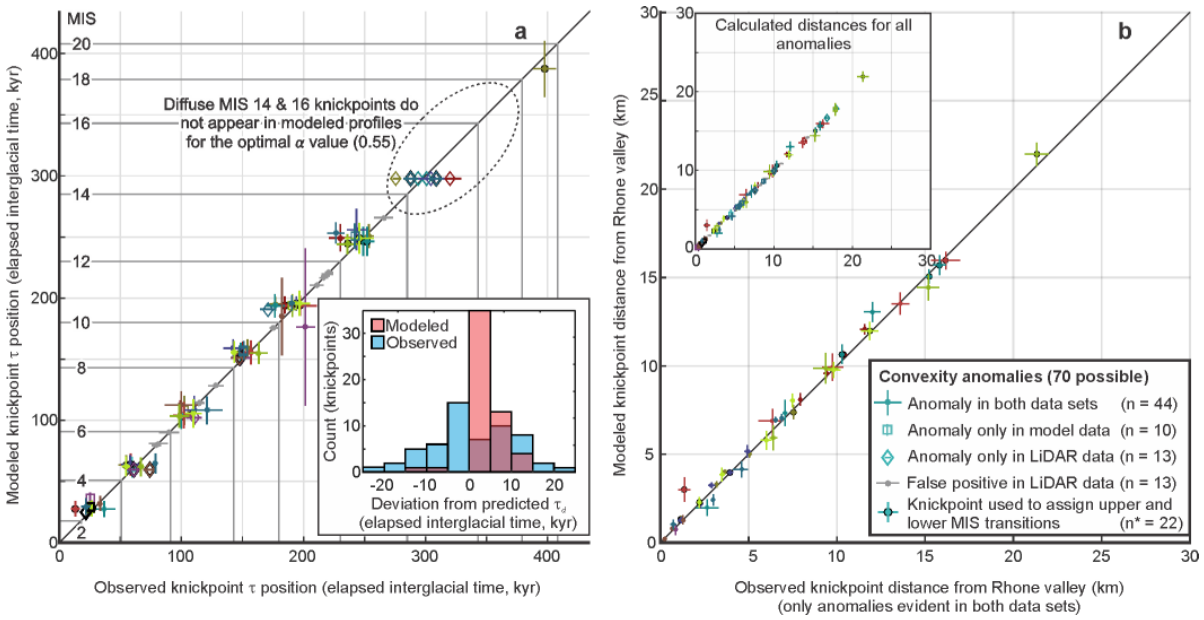

Fig 8 Comparison between locations of modelled and observed knickpoints for all channels in the study region. Anomalies represent the convex upstream extent of knickpoints within each catchment, and as such are located upstream of τ values corresponding to glacial-interglacial transitions responsible for knickpoint formation. Colours correspond to individual channels presented in Fig. S2; error bars indicate the length of each knickpoint within the respective profiles. Sections identified by high convexity, though discarded during automatic MIS allocation (see Appendix A) are plotted in grey along the 1:1 line. Locations used to assign upper and lower MIS transitions in our forward models are highlighted with black borders. Where knickpoints are identified in both profiles, points reflect the corresponding position, while knickpoints identified in only one profile are plotted against their predicted age (a), or on the 1:1 line (inset, b). We note that knickpoints used to assign upper and lower MIS transitions are re-located and assigned τ values using the same iterative search criteria as that for the remainder of the channel, thereby removing any bias from our initial selection parameters.

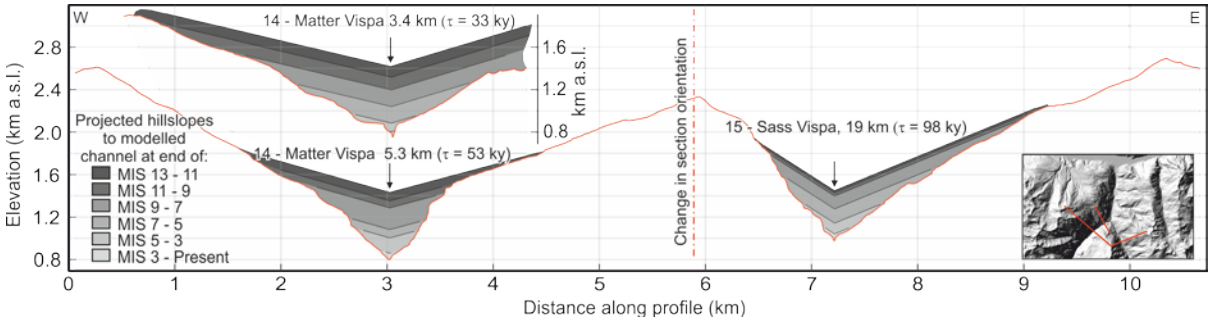

Fig. 9 Projection of strength-limited hillslopes from modelled end-of-interglacial channels to existing topography. LiDAR-derived cross-sections are situated to predominantly sample bedrock topography, and are typically steeper on the western side, where foliation dips into the topography. **Left:** The upper slopes of the 5.3 km Matter Vispa section demonstrate a strong correspondence to the initial model profile at MIS 13, while the V-shape and narrow inner gorge representing post-glacial incision are also apparent. Breaks in slope corresponding to modelled MIS 7, 5, and 3 are seen in the cross-section located at 3.4 km. Note the variation in model channel elevations between the two locations, reflecting the upstream progression of knickpoints from MIS 5, 7, and 3. **Right:** The south-western slope of the Saas Vispa section demonstrates profile breaks that correspond to modelled MIS 13, 7, 5, and 3 end-of-interglacial channel profiles, while the north-eastern slope is dominated by foliation-parallel bedrock instability.

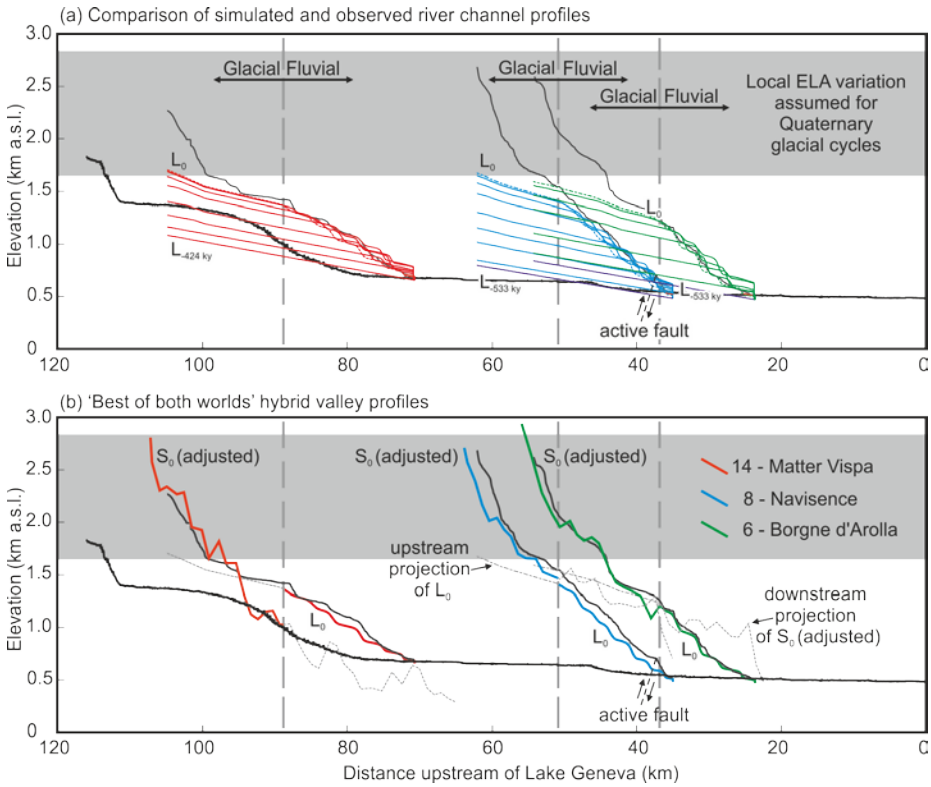

Fig. 10 Comparison of simulated and observed river channel profiles (a), and a 'best of both worlds' combination of fluvial and glacial models (b). Longitudinal profiles for valleys at the end of simulated glacial stages. S_0 and L_0 refer to the present-day elevation of the axis in Sternai et al. (2013) and this study, respectively. L_{-XXX} then refers to the profile of the modelled position of the valley floor at the initiation of our model runs. Black lines represent the profile of the Rhone Valley in the initial stage of both models. Vertical light grey lines represent the boundary between sections B and C in each catchment (considered to be the upstream extent of Pleistocene fluvial erosion). Dashed lines in (b) represent the projection of each model beyond the predicted extents of fluvial or glacial erosion, respectively.

Supplementary Materials

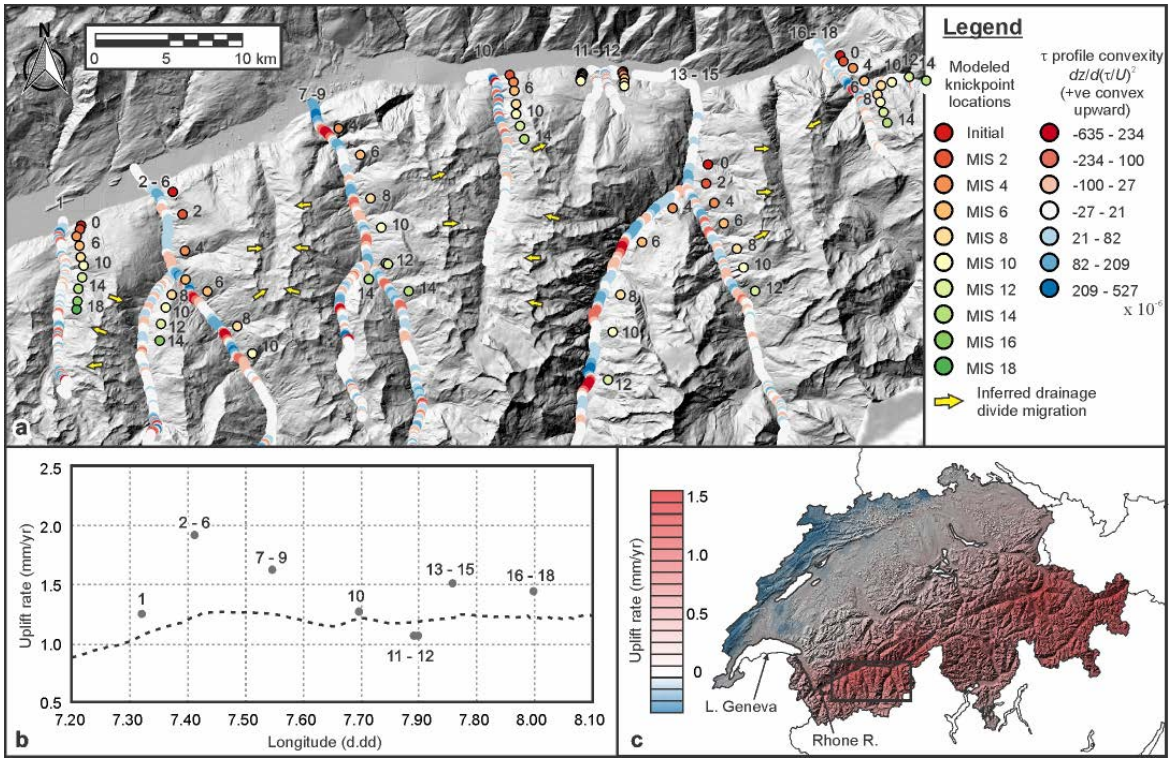

Fig. S1 Overview of observed and modelled knickpoint positions and uplift rates. a) Shaded relief map of the study region showing the location of present-day knickpoints evident from convexities in the channel profiles (in $z - \tau$ space), modelled knickpoint locations, and asymmetric ridges indicating drainage divide migration. **b**) Comparison of mean long-term uplift rates derived from our analysis of knickpoint sequences with present-day rates determined for catchment outlets along the southern side of the Rhone Valley (Brockmann et al., 2012). **c**) Present-day uplift map of Switzerland (Brockmann et al., 2012) indicating the location of the Rhone River, Lake Geneva, and the region of interest for this study.

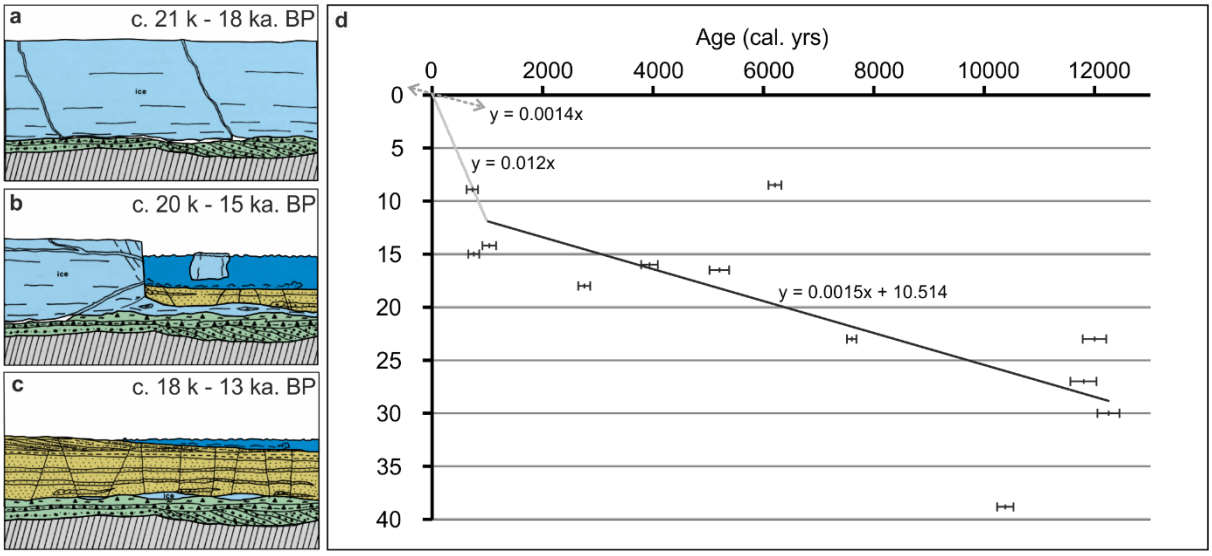

Fig. S2 Post-glacial infilling of the Rhone Valley and aggradation of the alluvial plane over the last 12 ka (modified after Finger and Weidmann, 1987; Hinderer, 2001; Pfiffner et al., 1997).

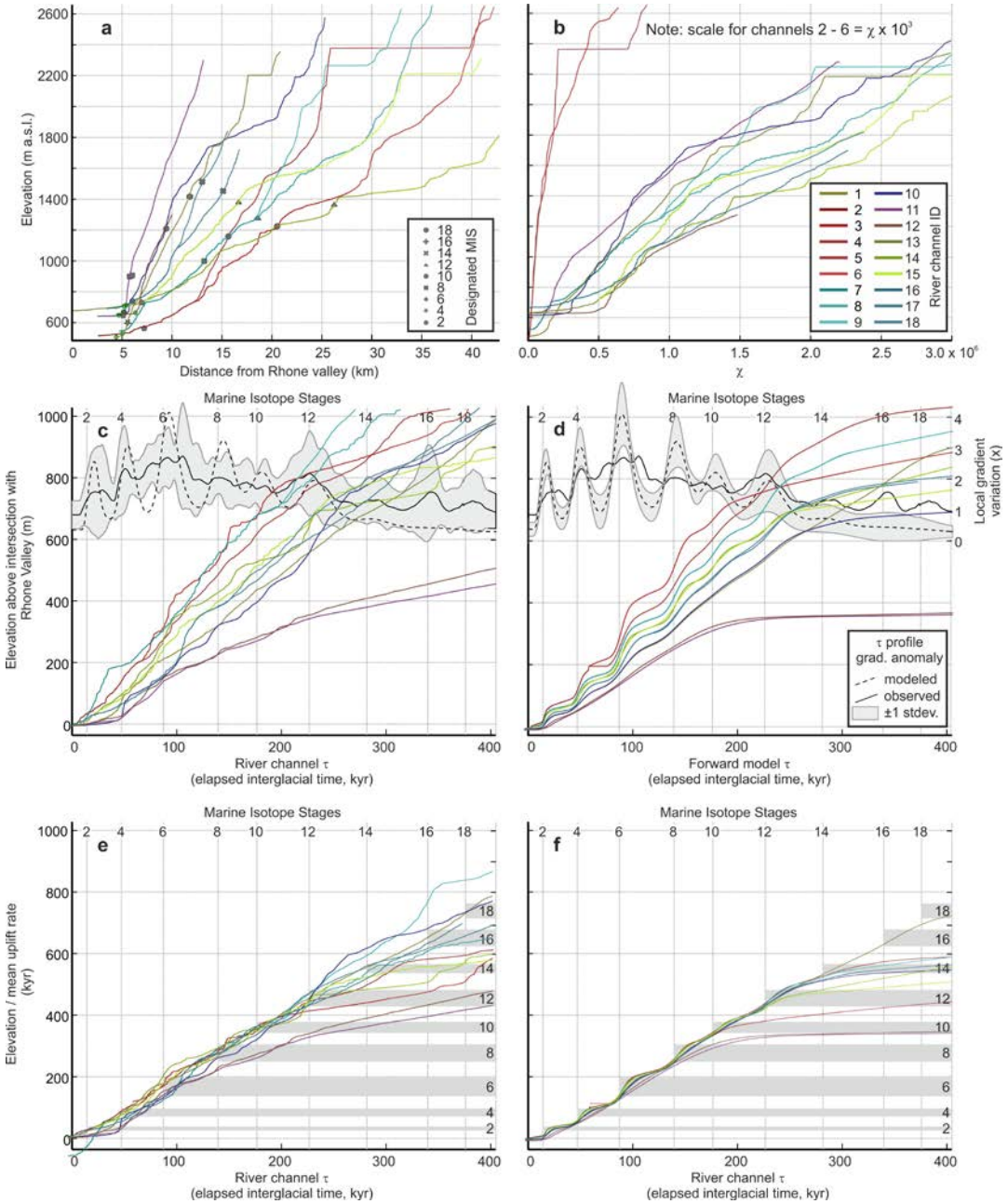

Fig. S3 Conversion of river profile information to a τ / z plot. a & b) River profiles are derived from a LiDAR DEM, and selected upper and lower knickpoints are identified in each channel along with designated marine isotope stages (a). χ plots generated to compare catchments independent of area (b). The χ axis for catchments 2 – 6 (m = 1.0, n = 1.0) is expanded for clarity. **c & d**) τ plots for all catchments. Elevations have been shifted to a common baselevel, while K and τ = 0 are determined to ensure upper and lower knickpoints correspond to appropriate marine isotope stages (c). τ plots for forward models derived from τ profiles (d) allows comparison between observed and predicted knickpoints. Local gradient anomalies (in τ / *(Z/U)* space) for the real and modelled profiles are plotted alongside data for comparison. **e & f**) Uplift-rate scaled τ plots for all catchments (e), and forward models (f). Cold MIS intervals are marked in grey.

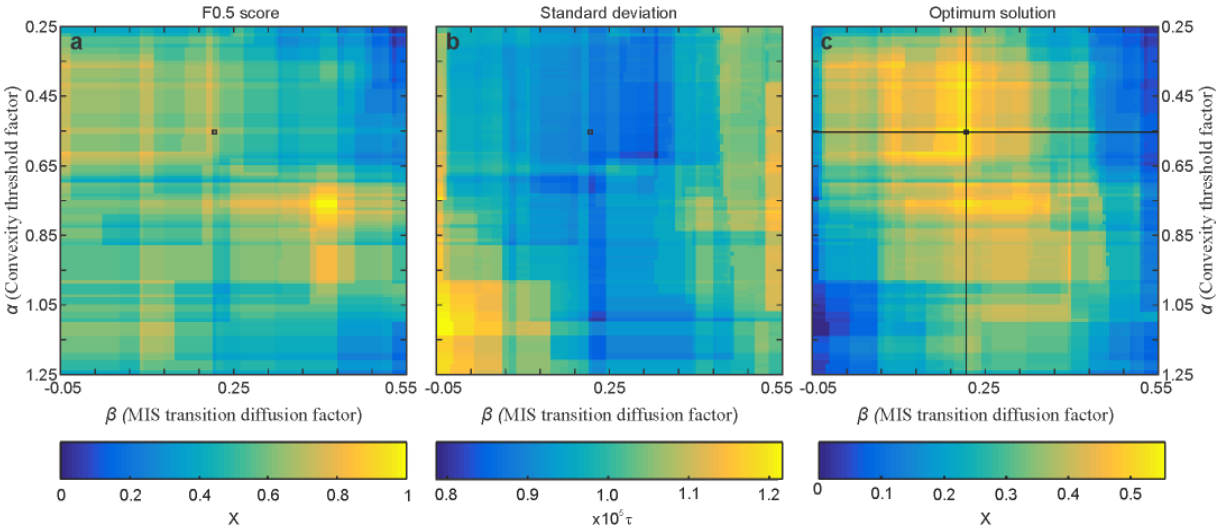

Fig. A1 Iterative search results used for determination of an optimal convexity threshold factor (α = 0.22) and MIS transition diffusion factor (β = 0.55). **a**) The F0.5 score provides a measure of the accuracy of knickpoint identification. **b**) The standard deviation describes the variance of calculated knickpoint ages (τ values) from the predicted knickpoint age adjusted for diffusion (τ_d). **c**). Our optimal combination of α and β.

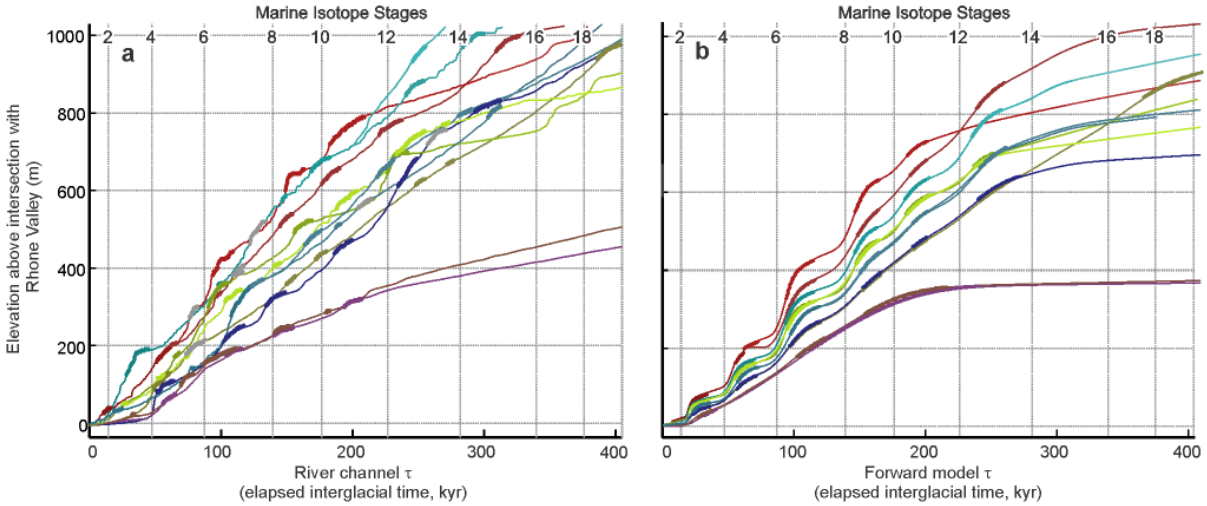

Fig. A2 τ plots for observed and modelled channels highlighting convexity anomalies in excess of the cutoff threshold determined from our iterative search. Colours correspond to individual channels presented in Figure S3. Thirteen identified high convexity sections discarded during automatic MIS allocation are plotted in grey.

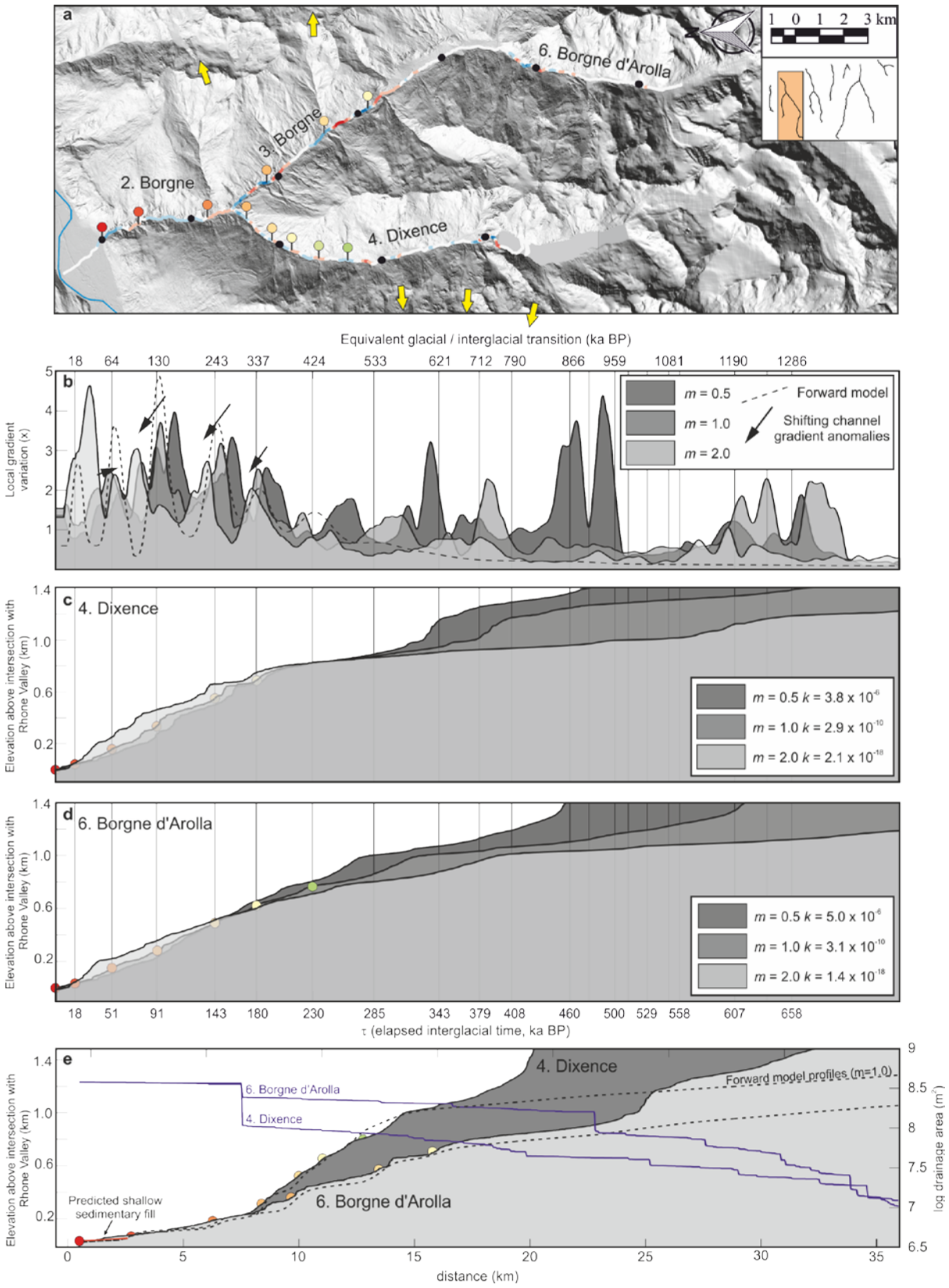

Fig. B1 Comparison of observed τ profiles from the Dixence and Borgne d'Arolla catchments for *m* = 0.5, 1.0, and 2.0. a) LiDAR-derived hillshade images. Channel colouring indicates calculated convexity (see Fig. S1 for colour scale), while circular markers indicate modelled τ values representing glacial intervals associated with knickpoint generation. Arrows indicate asymmetric ridges associated with likely drainage

divide migration. **b**) Mean channel gradient variation for the two catchments assuming different values of m. **c** & **d**) τ profiles for selected m values. The location of τ values corresponding to glacial intervals is indicated on the $m = 1$ profile for each catchment (see Fig. S1 for colour scale). **e**) Modelled and observed river profiles for the two catchments indicating the location of calculated knickpoint locations, and calculated extent of present-day sedimentary fill.

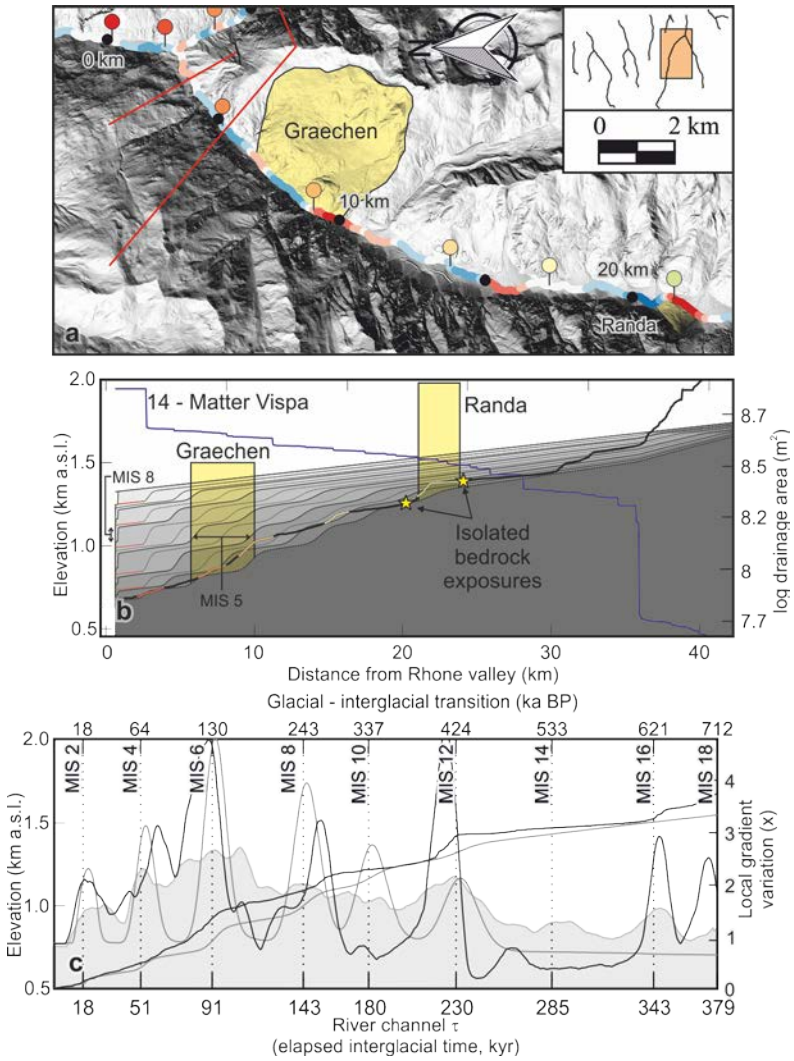

Fig. B2 Comparison of simulated and observed channel profiles in the Matter Vispa catchment affected by large landslides at Graechen and Randa. a) LiDAR-derived hillshade image of the reach indicating the location of the landslides in relation to the river channel. Channel colouring indicates calculated convexity (see Fig. S1 for colour scale), while circular markers indicate modelled τ values representing glacial intervals associated with knickpoint generation. **b**) Forward model stages calculated at each glacial – interglacial transition, and 20 ky intervals thereafter. Yellow shaded regions indicate the approximate position and elevation of landslides. Red lines denote sedimentary fill, while dashed profiles indicate the modelled present-day profile. Blue lines show catchment area, while coloured sections on the observed profiles highlight interpreted knickpoint locations. **c**) τ plots of observed (black) and modelled (grey) present-day channel profiles. Local gradient variations are also indicated, while the shaded background presents the mean gradient variation for all channels in our study region.

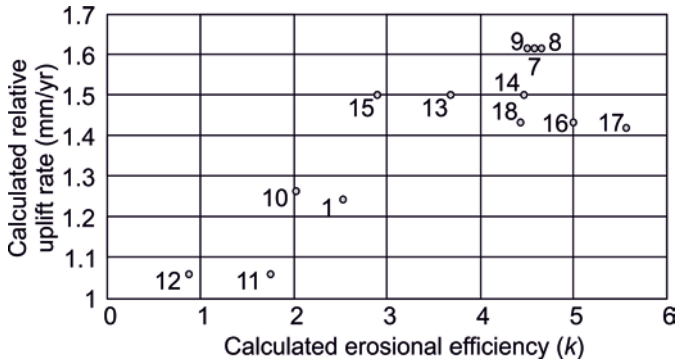

Fig. B3 Comparison of calculated erosional efficiency and relative uplift rate for catchments in the study area. Numbers represent individual river id's (see Fig. 1). Rivers 2 – 6 are excluded as our preferred *m* value does not equal 1.

REFERENCES

Bini, A., Buoncristiani, J.-F., Couterrand, S., Ellwanger, D., Felber, M., Florineth, D., Graf, H.R., Keller, O., Kelly, M., Schlüchter, C., Schoeneich, P., 2009. Switzerland during the Last Maximal (LGM). SwissTopo, Bern.

Brockmann, E., Ineichen, D., Marti, U., Schaer, S., Schlatter, A., Villiger, A., 2012. Determination of Tectonic Movements in the Swiss Alps Using GNSS and Levelling, in: Kenyon, S., Pacino, M.C., Marti, U. (Eds.), Geodesy for Planet Earth. Springer Berlin Heidelberg, pp. 689-695.

Burbank, D.W., Leland, J., Fielding, E., Anderson, R.S., Brozovic, N., Reid, M.R., Duncan, C., 1996. Bedrock incision, rock uplift and threshold hillslopes in the northwestern Himalayas. Nature 379, 505-510.

Burjánek, J., Fäh, D., Michel, C., Fäh, D., Fäh, D., 2012. Earthquake Damage Scenario in Visp (Switzerland): From Active Fault to Building Damage, 15th World Conference on Earthquake Engineering. ETH Zürich, Lisbon, pp. 5472 - 5481.

Champagnac, J.D., Schunegger, F., Norton, K., von Blanckenburg, F., Abbühl, L.M., Schwab, M.J., 2009. Erosion-driven uplift of the modern Central Alps. Tectonophysics 474, 236-249.

Cuffey, K.M., Paterson, W.S.B., 2010. The Physics of Glaciers, 4 ed. Academic Press.

Döppes, D., Rabeder, G., Stiller, M., 2011. Was the Middle Würmian in the High Alps warmer than today? Quaternary International 245, 193-200.

Duhnforth, M., Anderson, R.S., Ward, D., Stock, G.M., 2010. Bedrock fracture control of glacial erosion processes and rates. Geology 38, 423-426.

Egholm, D.L., Nielsen, S.B., Pedersen, V.K., Lesemann, J.-E., 2009. Glacial effects limiting mountain height. Nature 460, 884-887.

Escher, A., Masson, H., Steck, A., 1993. Nappe geometry in the Western Swiss Alps. Journal of Structural Geology 15, 501-509.

Finger, W., Weidmann, M., 1987. Quelques données géologiques nouvelles sur la vallée du Rhône entre Sierre et le Léman. Bulletin de la Murithienne 105, 27-40.

Fiore, J., Girardclos, S., Pugin, A., Gorin, G., Wildi, W., 2011. Würmian deglaciation of western Lake Geneva (Switzerland) based on seismic stratigraphy. Quaternary Science Reviews 30, 377-393.

Fox, M., Leith, K., Bodin, T., Balco, G., Shuster, D.L., 2015. Rate of fluvial incision in the Central Alps constrained through joint inversion of detrital 10Be and thermochronometric data. Earth and Planetary Science Letters 411, 27-36.

Häuselmann, P., Granger, D.E., Jeannin, P.-Y., Lauritzen, S.-E., 2007. Abrupt glacial valley incision at 0.8 Ma dated from cave deposits in Switzerland. Geology 35, 143-146.

Heim, A., 1885. Handbuch der Gletscherkunde. J. Engelhorn.

Hergarten, S., Wagner, T., Stüwe, K., 2010. Age and Prematurity of the Alps Derived from Topography. Earth and Planetary Science Letters 297, 453-460.

Herman, F., Beaud, F., Champagnac, J.-D., Lemieux, J.-M., Sternai, P., 2011. Glacial hydrology and erosion patterns: A mechanism for carving glacial valleys. Earth and Planetary Science Letters 310, 498-508.

Hinderer, M., 2001. Late Quaternary denudation of the Alps, valley and lake fillings and modern river loads. Geodinamica Acta 14, 231-263.

Howard, A.D., Dietrich, W.E., Seidl, M.A., 1994. Modeling fluvial erosion on regional to continental scales. J. Geophys. Res. 99, 13971-13986.

Jansen, J.D., Codilean, A.T., Stroeven, A.P., Fabel, D., Hättestrand, C., Kleman, J., Harbor, J.M., Heyman, J., Kubik, P.W., Xu, S., 2014. Inner gorges cut by subglacial meltwater during Fennoscandian ice sheet decay. Nat Commun 5.

Koppes, M., Hallet, B., Rignot, E., Mouginot, J., Wellner, J.S., Boldt, K., 2015. Observed latitudinal variations in erosion as a function of glacier dynamics. Nature 526, 100-103.

Koppes, M.N., Montgomery, D.R., 2009. The relative efficacy of fluvial and glacial erosion over modern to orogenic timescales. Nature Geoscience 2, 644-647.

Korup, O., Schlunegger, F., 2007. Bedrock landsliding, river incision, and transience of geomorphic hillslope-channel coupling: Evidence from inner gorges in the Swiss Alps. J. Geophys. Res. 112.

Leith, K., Moore, J.R., Amann, F., Loew, S., 2014. Sub-glacial extensional fracture development and implications for Alpine valley evolution. J. Geophys. Res. 119, 62-81.

Lisiecki, L., Raymo, M.E., 2005. A Pliocene-Pleistocene stack of 57 globally distributed benthic $\delta^{18}O$ records. Palaeoceanography 20, 1-17.

Mey, J., Scherler, D., Wickert, A.D., Egholm, D.L., Tesauro, M., Schildgen, T.F., Strecker, M.R., 2016. Glacial isostatic uplift of the European Alps. Nature Communications 7, 13382.

Montgomery, D.R., Korup, O., 2010. Preservation of inner gorges through repeated Alpine glaciations. Nature Geoscience 4, 62-67.

Muttoni, G., Ravazzi, C., Breda, M., Pini, R., Laj, C., Kissel, C., Mazaud, A., Garzanti, E., 2007. Magnetostratigraphic dating of an intensification of glacial activity in the southern Italian Alps during Marine Isotope Stage 22. Quaternary Research 67, 161-173.

Penck, A., Brückner, E., 1909. Die Alpen im Eiszeitalter, Leipzig.

Petit, C., Goren, L., Rolland, Y., Bourlès, D., Braucher, R., Saillard, M., Cassol, D., 2017. Recent, climate-driven river incision rate fluctuations in the Mercantour crystalline massif, southern French Alps. Quaternary Science Reviews 165, 73-87.

Pfiffner, O.A., Heitzmann, P., Lehner, P., Frei, W., Pugin, A., Felber, M., 1997. Incision and backfilling of Alpine valleys: Pliocene, Pleistocene and Holocene processes, NFP20-Atlas: Deep structure of the Swiss Alps.

Preusser, F., Reitner, J., Schlüchter, C., 2010. Distribution, geometry, age and origin of overdeepened valleys and basins in the Alps and their foreland. Swiss Journal of Geosciences 103, 407-426.

Roberts, G.G., White, N., 2010. Estimating uplift rate histories from river profiles using African examples. J. Geophys. Res. 115, B02406.

Robl, J., Prasicek, G., Hergarten, S., Stüwe, K., 2015. Alpine topography in the light of tectonic uplift and glaciation. Global and Planetary Change.

Royden, L., Perron, T.J., 2013. Solutions of the stream power equation and application to the evolution of river longitudinal profiles. J. Geophys. Res. 118, 497-518.

Schmid, S.M., Pfiffner, O.A., Froitzheim, N., Schönborn, G., Kissling, E., 1996. Geophysical-geological transect and tectonic evolution of the Swiss-Italian Alps. Tectonics 15, 1036-1064.

Selby, M.J., 1982. Controls on the stability and inclinations of hillslopes formed on hard rock. Earth Surface Processes and Landforms 7, 449-467.

Serpelloni, E., Faccenna, C., Spada, G., Dong, D., Williams, S.D.P., 2013. Vertical GPS ground motion rates in the Euro-Mediterranean region: New evidence of velocity gradients at different spatial scales along the Nubia-Eurasia plate boundary. Journal of Geophysical Research: Solid Earth 118, 6003-6024.

Shuster, D.L., Cuffey, K.M., Sanders, J.W., Balco, G., 2011. Thermochronometry reveals headward propagation of erosion in an alpine landscape. Science 332, 84-88.

Shuster, D.L., Ehlers, T.A., Rusmoren, M.E., Farley, K.A., 2005. Rapid Glacial Erosion at 1.8 Ma Revealed by $^{4}He/^{3}He$ Thermochronometry. Science 310, 1668-1670.

Spicher, A., 2005. Geological Map of Switzerland. Geological Institute, University of Bern, and Federal Office for Water and Geology.

Steck, A., Hunziker, J., 1994. The Tertiary structural and thermal evolution of the Central Alps--compressional and extensional structures in an orogenic belt. Tectonophysics 238, 229-254.

Sternai, P., Herman, F., Valla, P.G., Champagnac, J.-D., 2013. Spatial and temporal variations of glacial erosion in the Rhône valley (Swiss Alps): Insights from numerical modeling. Earth and Planetary Science Letters 368, 119-131.

Tucker, G.E., Whipple, K.X., 2002. Topographic outcomes predicted by stream erosion models: Sensitivity analysis and intermodel comparison. J. Geophys. Res. 107, 2179.

Valla, P.G., Shuster, D.L., van der Beek, P.A., 2011. Significant increase in relief of the European Alps during mid-Pleistocene glaciations. Nature Geosci 4, 688-692.

Valla, P.G., van der Beek, P.A., Lague, D., 2010. Fluvial incision into bedrock: Insights from morphometric analysis and numerical modeling of gorges incising glacial hanging valleys (Western Alps, France). J. Geophys. Res. 115, F02010.

Valla, P.G., van der Beek, P.A., Shuster, D.L., Braun, J., Herman, F., Tassan-Got, L., Gautheron, C., 2012. Late Neogene exhumation and relief development of the Aar and Aiguilles Rouges massifs (Swiss Alps) from low-temperature thermochronology modeling and $^{4}He/^{3}He$ thermochronometry. J. Geophys. Res. 117, F01004.

Whipple, K.X., Tucker, G.E., 1999. Dynamics of the stream-power river incision model: Implications for height limits of mountain ranges, landscape response timescales, and research needs. J. Geophys. Res. 104, 17661-17674.

Whittaker, A.C., 2012. How do landscapes record tectonics and climate? Lithosphere 4, 160-164.

Willett, S.D., McCoy, S.W., Perron, J.T., Goren, L., Chen, C.-Y., 2014. Dynamic Reorganization of River Basins. Science 343.

Wittmann, H., von Blanckenburg, F., Kruesmann, T., Norton, K.P., Kubik, P.W., 2007. Relation between rock uplift and denudation from cosmogenic nuclides in river sediment in the Central Alps of Switzerland. J. Geophys. Res. 112.